1997

Intergalactic helium absorption in cold dark matter models

RAC Croft

DH Weinberg

N Katz

L Hernquist

Intergalactic Helium Absorption in Cold Dark Matter Models

Rupert A.C. Croft[1,6], David H. Weinberg[1,7], Neal Katz[2,3,8], and Lars Hernquist[4,5,9]

ABSTRACT

Observations from the Hopkins Ultraviolet Telescope and the Hubble Space Telescope have recently detected HeII absorption along the lines of sight to two high redshift quasars. We use cosmological simulations with gas dynamics to investigate HeII absorption in the cold dark matter (CDM) theory of structure formation. We consider two $\Omega = 1$ CDM models with different normalizations and one open universe ($\Omega_0 = 0.4$) CDM model. The simulations incorporate the photoionizing UV background spectrum computed by Haardt & Madau (1996), which is based on the output of observed quasars and reprocessing by the Lyα forest. The simulated gas distribution, combined with the Haardt & Madau spectral shape, accounts for the relative observed values of $\overline{\tau}_{\rm HI}$ and $\overline{\tau}_{\rm HeII}$, the effective mean optical depths for HI and HeII absorption. If the background intensity is as high as Haardt & Madau predict, then matching the absolute observed values of $\overline{\tau}_{\rm HI}$ and $\overline{\tau}_{\rm HeII}$ requires a baryon abundance larger (by factors between 1.5 and 3 for the various CDM models) than our assumed value of $\Omega_b h^2 = 0.0125$. The simulations reproduce the evolution of $\overline{\tau}_{\rm HeII}$ over the observed redshift range, $2.2 \lesssim z \lesssim 3.3$, if the HeII photoionization rate remains roughly constant.

HeII absorption in the CDM simulations is produced by a diffuse, fluctuating, intergalactic medium, which also gives rise to the HI Lyα forest. Much of the HeII opacity arises in underdense regions where the HI optical depth is very low. We compute statistical properties of the HeII and HI absorption that can be used to test the CDM models and distinguish them from an alternative scenario in which the HeII absorption is caused by discrete, compact clouds. The CDM scenario predicts that a substantial amount of baryonic material resides in underdense regions at high redshift.

[1]Department of Astronomy, The Ohio State University, Columbus, OH 43210

[2] Department of Astronomy, University of Washington, Seattle, WA, 98195

[3] Department of Physics and Astronomy, University of Massachusetts, Amherst, MA, 98195

[4]Lick Observatory, University of California, Santa Cruz, CA 95064

[5]Presidential Faculty Fellow

[6]racc@astronomy.ohio-state.edu

[7]dhw@astronomy.ohio-state.edu

[8]nsk@kestrel.phast.umass.edu

[9]lars@helios.ucolick.org

HeII absorption is the only sensitive observational probe of such extremely diffuse, intergalactic gas, so it can provide a vital test of this fundamental prediction.

Subject headings: quasars: absorption lines, Galaxies: formation, large-scale structure of Universe

1. Introduction

The Lyman-α forest seen in quasar spectra (Lynds 1971; Sargent et al. 1980) is produced by absorption from diffuse hydrogen at high redshift. The big bang model predicts that approximately 25% of primordial baryonic matter should also be in the form of helium, and that there should therefore be corresponding absorption at shorter wavelengths from the Lyα transition of singly ionized helium (HeII). It has recently become possible to detect redshifted HeII absorption with space-based, ultraviolet (UV) observations (Jakobsen et al. 1994; Davidsen, Kriss, & Zheng 1996; Hogan, Anderson, & Rugers 1996). Recent hydrodynamic cosmological simulations of cold dark matter (CDM) models have been remarkably successful in reproducing the observed properties of the HI Lyα forest (Cen et al. 1994; Zhang, Anninos, & Norman 1995; Hernquist et al. 1996, hereafter HKWM; Miralda-Escudé et al. 1996; Davé et al. 1997; Zhang et al. 1997, Rauch et al. 1997). In this paper we examine whether simulations like those of HKWM can also account for the observed HeII absorption, and we consider their implications for the physical state of the absorbing gas.

The basic physics of intergalactic HeII absorption is elegantly described by Miralda-Escudé (1993). The ambient background of UV radiation produced by quasars and (perhaps) young galaxies keeps the diffuse hydrogen of the Lyα forest in a highly photoionized state, and it also ensures that most diffuse helium is singly or doubly ionized. However, the UV background intensity is lower at the ionization energy of HeII (4 Rydbergs, 228$\mathring{A}$) than it is at the HI ionization energy (1 Rydberg, 912$\mathring{A}$), and HeII absorption can therefore be significant even in regions where the HI density is very low. HeII absorption may be the only practical tool for directly observing regions that lie significantly below the cosmic mean density, revealing gas whose hydrogen Lyα absorption might be buried in noise or removed in the process of continuum fitting. According to gravitational instability models of structure formation, the voids between galaxies should harbor a substantial portion of the baryonic matter in the universe. A homogeneous intergalactic medium (IGM) would produce a uniform absorption trough in quasar spectra (Gunn & Peterson 1965). In a realistic gravitational instability model, the matter in underdense regions should instead produce a fluctuating continuum of absorption (Reisenegger & Miralda-Escudé 1995).

Once the hydrogen in the universe has been reionized, the neutral helium fraction is expected to be small except in high density, collapsed regions. At fixed density and temperature, the

fraction of HeII in highly photoionized gas is inversely proportional to the photoionization rate,

$$\Gamma_{\rm HeII} = \int_{\nu_{\rm HeII}}^{\infty} d\nu \frac{4\pi J(\nu)}{h\nu} \sigma_{\rm HeII}(\nu), \tag{1}$$

where $J(\nu)$ is the specific intensity of the background at frequency ν, $\sigma_{\rm HeII}$ is the ionization cross section for HeII, and $h\nu_{\rm HeII} = 4$ Rydbergs. The HI fraction is inversely proportional to

$$\Gamma_{\rm HI} = \int_{\nu_{\rm HI}}^{\infty} d\nu \frac{4\pi J(\nu)}{h\nu} \sigma_{\rm HI}(\nu), \tag{2}$$

which is dominated by photons with energy between 1 and 4 Rydbergs. Measurements of the mean HeII and HI Lyα opacities can constrain the spectral shape of the UV background through the ratio of these integrals, $\Gamma_{\rm HI}/\Gamma_{\rm HeII}$, provided one has a model that specifies the density and temperature structure of the absorbing gas. The evolution of the UV background's intensity and shape can be tracked by the evolution of the mean opacities with redshift. The simulations provide a realistic model for the IGM with the physical detail needed to exploit this approach, albeit a model whose properties depend (as they should) on the parameters of the underlying cosmological scenario.

For a given cosmological model, or indeed for any model IGM in which most of the absorption arises in highly photoionized gas, the predicted mean opacity depends on the parameter combination Ω_b^2/Γ, where Ω_b is the baryon density parameter (e.g., Miralda-Escudé and Ostriker 1992). This scaling assumes that gas temperatures (and hence recombination rates) are unaffected by changes in Ω_b and Γ, an assumption that we will revisit in §3.2. The simulations allow us to ask whether a cosmological model is consistent with the observed mean opacities given constraints on Ω_b from big bang nucleosynthesis (e.g., Walker et al. 1991) and on Γ from the observed quasar population (e.g., Haardt & Madau 1996) or the proximity effect (e.g., Bajtlik, Duncan, & Ostriker 1988). The simulations also predict distribution functions for HI and HeII opacities and for the ratio of these opacities, which can be compared to observations in order to test the simulated IGM.

The possiblity of detecting HeII absorption from diffuse intergalactic gas was one of the main scientific motivations for the Hopkins Ultraviolet Telescope (HUT), which first flew on the Astro-1 mission in 1990 (Davidsen, private communication). While the quasar absorption experiment could not be carried out during Astro-1, because of pointing problems, it was successfully performed during the Astro-2 mission in 1995, as described by Davidsen, Kriss & Zheng (1996, hereafter DKZ). The first detection of HeII absorption was in fact achieved before Astro-2 by Jakobsen et al. (1994, hereafter JBDGJP), who used the HST Faint Object Camera to observe the quasar Q0302-003 (z=3.28). They measured a clear drop in the received quasar continuum across the 304$\mathring{A}$ (rest-frame) edge, and they inferred a high HeII optical depth, $\tau_{\rm HeII} > 1.7$ at 90% confidence. Because of the relatively low spectral resolution, the authors were unable to establish whether the absorption was caused mainly by material associated with individually identified HI lines or by a more diffuse component. JBDGJP, Giroux, Fardal, & Shull (1995), Madau & Meiksin (1995), and Songaila, Hu, & Cowie (1995) have explored the implications of these data for the shape of

the UV background spectrum assuming different analytic models of the absorbing medium. If the absorption is dominated by discrete lines, then the spectrum must be quite soft, but a harder spectrum is allowed if most HeII absorption arises in a diffuse, "Gunn-Peterson" background. We qualify this latter term with scare-quotes because the analytic models typically assume a uniform Gunn-Peterson effect, while the cosmological simulations predict a smoothly fluctuating, diffuse IGM that blurs the traditional distinction between Gunn-Peterson absorption and the Lyα forest (HKWM; see also Miralda-Escudé & Rees 1993; Cen et al. 1994; Miralda-Escudé et al. 1996).

Q0302-003 was recently reobserved by Hogan et al. (1996, hereafter HAR), using the Goddard High Resolution Spectrograph on HST. HAR confirm JBDGJP's detection of HeII absorption, but the higher spectral resolution of the GHRS observations reveals interesting new details. The transmission below the HeII break remains fairly high (~ 0.3) within about 4000 km s^{-1} of the quasar. HAR attribute the relatively low HeII fraction in this region to photoionization caused by Q0302-003 itself, with the ionization zone terminated by a high column density HI absorber. They find a low but significant level of residual flux at shorter wavelengths corresponding to $\tau_{\rm HeII} = 2.0^{+1.0}_{-0.5}$ at 95% confidence. The upper limit on $\tau_{\rm HeII}$ implies that helium remains predominantly doubly ionized even outside of the ionization zone produced by Q0302-003, presumably because of the ambient UV background. The upper limit depends on accurate background subtraction at the blue end of the spectrum, a challenging problem that is discussed in detail by HAR.

HST cannot probe HeII absorption below $z \approx 3$. DKZ took advantage of the shorter wavelength sensitivity of the HUT to measure HeII absorption in the spectrum of HS1700+64 (z=2.743). They find a mean opacity in the redshift range $2.2 < z < 2.6$ corresponding to $\tau_{\rm HeII} = 1.0 \pm 0.07$, with some evidence that the opacity increases as a function of redshift over this range. The observed wavelength interval is $\sim 150\AA$ and the spectral resolution $\sim 3\AA$, so the HUT spectrum contains enough information to reveal structure in the residual flux. (The spectrum shown in DKZ is averaged in $10\AA$ bins.) The analysis in this paper will be aimed primarily at the HUT observations. The physical issues are rather different for Q0302-003 because of the important role of the observed quasar itself in ionizing the absorbing gas. We will therefore save a detailed comparison to the JBDGJP and HAR observations for a future paper.

The numerical approach in this paper will be similar to that of HKWM, who use smoothed-particle hydrodynamics (SPH) simulations to study the HI Lyα forest in a critical density, CDM universe. Studies of HeII (and HI) absorption in Eulerian-grid hydrodynamic simulations have been carried out by Zhang et al. (1995, 1996) and Miralda-Escudé et al. (1996). Here we will study the physical state of the gas that produces HeII absorption in CDM-dominated, gravitational instability models of structure formation, relating it to and differentiating it from the gas that dominates HI absorption. We will use information on HeII and HI in the context of these models to study the required UV background spectrum, its evolution with redshift, and the implied baryon density. We will examine several variants of the CDM scenario, enabling us to see which features are generic within this cosmological picture and which can be used as diagnostics for

constraining cosmological parameters. We will also compare the simulation results to those of a simple model where all of the flux is absorbed in discrete lines. This sort of model is often used as a phenomenological description of the HI Lyα forest, though it does not correspond physically to what happens in the simulations, where the absorbing structures are relatively diffuse and merge continuously into a fluctuating background. We obtain predictions that can be compared to future observational analyses that probe HI and HeII absorption along a common line of sight.

2. Simulations

We have used the N-body plus SPH code TreeSPH (Hernquist & Katz 1989; Katz, Weinberg, & Hernquist 1996, hereafter KWH) to simulate three different CDM-dominated cosmological models, the parameters of which are listed in columns $2-5$ of Table 1. The first is a "standard" CDM (SCDM) universe, with $\Omega = 1$, $h = 0.5$ (where $h \equiv H_0/100$ km s^{-1} Mpc^{-1}), and $\Omega_b = 0.05$. The power spectrum is normalized so that the rms amplitude of mass fluctuations in 8 h^{-1}Mpc spheres, linearly extrapolated to $z = 0$, is $\sigma_8 = 0.7$. This normalization is consistent with that advocated by White, Efstathiou & Frenk (1993) to match the observed masses of rich galaxy clusters, but it is inconsistent with the normalization implied by the COBE-DMR experiment. Our second model is identical to the first except that $\sigma_8 = 1.2$. This higher amplitude is consistent with the 4-year COBE data (Bennett et al. 1996), and we therefore label the model CCDM. The third model, OCDM, assumes an open universe with $\Omega_0 = 0.4$, $h = 0.65$ and $\Omega_b = 0.03$. The transfer functions used are those of Efstathiou, Bond & White 1992. The shape parameter $\Gamma = 0.234$ was used for the OCDM model, which is also COBE-normalized ($\sigma_8 = 0.75$, Gorski et al. 1995). The baryon fraction for these models, $\Omega_b = 0.0125h^{-2}$, was chosen based on the big bang nucleosynthesis analysis of Walker et al. (1991), who deduce primordial abundances of D, ^{3}He, ^{4}He, and ^{7}Li from local observations using models for chemical processing of elements in stars. Measurement of the deuterium abundance in high redshift Lyman limit systems offers a more direct route to determining $\Omega_b h^2$. The first applications of this method have so far given results which favor $\Omega_b h^2$ being a factor of ~ 2 smaller (Carswell et al. 1994; Songaila et al. 1994; Rugers & Hogan 1996ab, but see also Hogan 1997) or a factor of ~ 2 larger (Tytler, Fan & Burles 1996, Tytler, Burles & Kirkman 1996, but see also Songaila, Wampler & Cowie 1996). The observational situation is thus uncertain at present, though we shall see that the high $\Omega_b h^2$ results are favored in the CDM models.

A periodic cubic volume of comoving side length 11.111 h^{-1}Mpc was simulated for each model, each simulation having identical random phases and being evolved to $z = 2$. We analyzed outputs at $z = 3.5, 3.0, 2.67, 2.33$ and 2, encompassing the range of existing HeII absorption observations. Each simulation was run with 64^3 collisionless dark matter particles and 64^3 gas particles. A spatially uniform photoionizing radiation field was imposed, and radiative cooling and heating rates were calculated assuming photoionization equilibrium and optically thin gas, as discussed in KWH. The spectral shape of the background radiation field and its evolution with

redshift were taken from the work of Haardt & Madau (1996, hereafter HM). This background was calculated by HM from a self-consistent treatment of the absorption and re-emission of light from observed quasars by the Lyα forest.

The implementation of photoionization in TreeSPH requires values of the photoionization rates and photoionization heating rates for HI, HeI, and HeII as a function of redshift (see Katz, Weinberg, & Hernquist 1996). We compute these parameters from the HM spectrum at intervals $\Delta z = 0.05$, and for the simulations we use fitting formulae that match these values to within $\sim 10\%$. The parameters that are particularly relevant for this paper are the photoionization rates $\Gamma_{\rm HI}$ and $\Gamma_{\rm HeII}$, for which we adopt

$$_{\rm HM}\Gamma_{\rm HI} = 1.115 \times 10^{-12} \exp\left[-0.57565(z-2.5)^2\right] \, {\rm s}^{-1}, \tag{3}$$

$$_{\rm HM}\Gamma_{\rm HeII} = 1.088 \times 10^{-14} \exp\left[-0.57565(z-2.5)^2\right] P(z) \, {\rm s}^{-1}, \tag{4}$$

where the factor

$$P(z) = 1 + 0.125(z-2.5) + 0.0825(z-2.5)^2 \tag{5}$$

accounts for the slight difference in the relative evolution of $\Gamma_{\rm HI}$ and $\Gamma_{\rm HeII}$. At $z \sim 2-4$, the values implied by equations (3) and (4) are about 30% lower than those shown in figure 6 of HM because we fit HM's $q_0 = 0.5$ results rather than their $q_0 = 0.1$ results (see §5.13 of HM). We set the UV background to zero at $z > 6$, since observations suggest that the population of quasars is already declining rapidly between $z = 4$ and $z = 5$. As shown by Hui & Gnedin (1997), the thermal state of the IGM at $z \lesssim 3$ is insensitive to the epoch of reionization provided that it occurs at $z \gtrsim 5$. If HI or HeII reionization occurs at $z < 5$, the IGM could be somewhat hotter than our simulations predict, a point that we will return to at the end of §3.4.

The HKWM results suggested that a simulation with the HM background and $\Omega_b = 0.05$ would underproduce the observed HI Lyα opacity, and we therefore reduced the amplitude of the HM background by a factor of two (i.e. to half the values implied by equations 3 and 4) before evolving the simulations. We can recover the impact of different UV background intensities at the analysis stage, regardless of the specific value adopted during dynamical evolution, as discussed below in §3.1. The SCDM simulation of this paper is identical to the simulation analyzed by

Table 1: Parameters of cosmological models. The conventions are defined in §2, except for C which is defined in equation (7).

model	Ω_0	h	Ω_b	σ_8	$C_{\rm HeII}$ $(z = 2-3.3)$	$C_{\rm HI}(z=2)$	$C_{\rm HI}(z=3)$
SCDM	1	0.5	0.05	0.7	3.0	2.6	2.8
CCDM	1	0.5	0.05	1.2	8.0	5.7	6.7
OCDM	0.4	0.65	0.03	0.75	3.0	2.4	2.8

HKWM except for the UV background spectrum (HKWM used a ν^{-1} power-law) and the inclusion of star formation (using the prescription of KWH). Star formation and the associated feedback only influence the simulation results in high density regions that are not the focus of this paper.

The UV background determines the relative fractions of different ionic species at specified density and temperature. Figure 1 shows the fractions of HI, HeI, and HeII as a function of temperature for (total) hydrogen densities $n_H = 3.95\times10^{-6}$ cm^{-3} (left panel) and 3.95×10^{-5} cm^{-3} (right panel). These are, respectively, the mean density and an overdensity of 10 at $z = 2.33$ for $\Omega_b h^2 = 0.0125$. We will focus much of our analysis on this redshift because it is the simulation output closest to the middle of DKZ's observed redshift range. Abundances are computed by requiring balance between the production and destruction rates for each species, as described in KWH. Thin lines show abundances for no UV background — these collisional equilibrium abundances depend on temperature alone and are thus the same in the two panels. Thick lines show abundances for the HM background, with intensity reduced by a factor of three (relative to HM), the value required for our SCDM and OCDM models to reproduce the observed HeII opacity (see §3.1). Photoionization dominates completely over collisional ionization at low temperatures, where the HI and HeII fractions fall as $T^{-0.7}$ because of the temperature dependence of the recombination rates. Collisional ionization becomes significant at high temperatures. Raising the density increases the recombination rates and, therefore, the HI, HeI, and HeII fractions, though these never exceed their collisional equilibrium values. Lowering the UV background by a constant factor would have the same effect on these plots as raising the density by the same factor.

The *shape* of the background spectrum determines the relative fractions of HI and HeII through the ratio of photoionization rates, $\Gamma_{\rm HI}/\Gamma_{\rm HeII}$. HM assume a $\nu^{-1.5}$ power-law for the intrinsic UV spectrum of their quasar sources, but the ambient background that they compute is substantially softer because of reprocessing by the Lyα forest. In particular, the spectrum at $z \sim 2.5$ drops by a factor ~ 15 at $h\nu \sim 4$ Rydbergs because of HeII absorption. If we adopted a pure $\nu^{-1.5}$ power-law with intensity chosen to produce the HI fractions in Figure 1, the HeII fractions at low temperatures would be reduced by a factor of 3.3. With the ν^{-1} power-law of HKWM, the reduction would be a factor of 6.5. It is worth noting, however, that these changes in equilibrium abundances have no dynamical impact on the simulations and minimal impact on the ability of the gas to cool in collapsed objects. The fraction of gas that cools and condenses into galaxies is nearly identical in simulations with the HM background and a ν^{-1} background (Weinberg, Hernquist, & Katz 1996).

3. Results

The Lyα optical depth produced by a uniform medium with neutral hydrogen or singly ionized helium density n is (Gunn & Peterson 1965; Miralda-Escudé 1993)

$$\tau = \frac{\pi e^2}{m_e c} f \lambda H^{-1}(z) n, \tag{6}$$

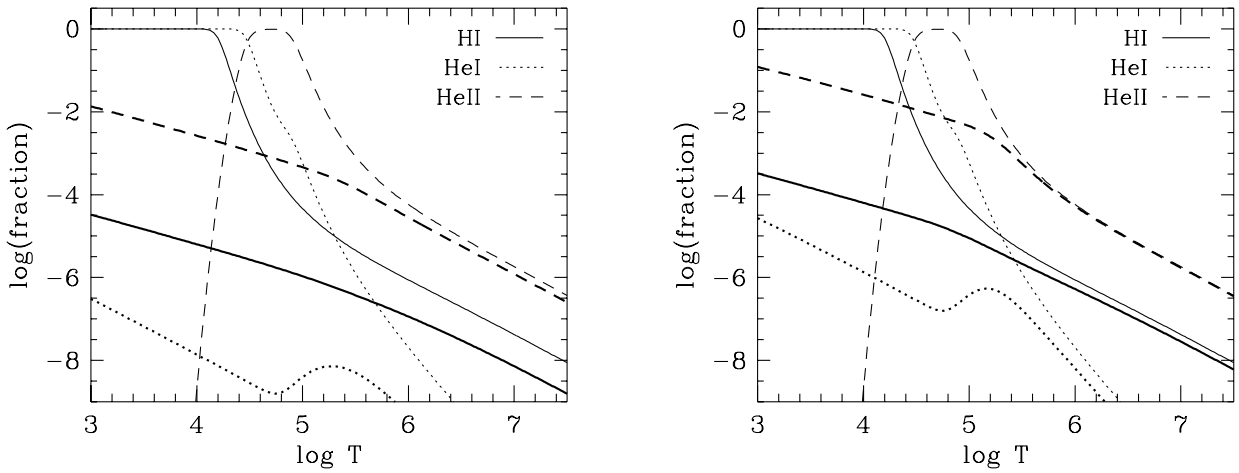

Fig. 1.— Fractions of HI (solid lines), HeI (dotted lines), and HeII (dashed lines) as a function of gas temperature. The assumed gas densities are $n_H = 3.95 \times 10^{-6}$ cm^{-3} in the left panel (the mean density at $z = 2.33$ for $\Omega_b h^2 = 0.0125$) and a factor of ten higher in the right panel. Thin lines show collisional equilibrium abundances. Thick lines show abundances in photoionization equilibrium with a UV background that has the spectral shape computed by HM but an intensity lower by factor of three.

where $H(z)$ is the Hubble constant at redshift z, $f = 0.416$ is the Lyα oscillator strength, and λ is the transition wavelength ($1216\mathring{A}$ and $304\mathring{A}$ for HI and HeII, respectively). In the simulations, the intergalactic gas is not uniform, so the optical depth varies as a function of wavelength and angular position. Figure 2 shows HI and HeII "absorption maps" of a slice through the center of the SCDM simulation at $z = 2.33$. (the velocity width of the full cube is 2029 km s^{-1} at this redshift). The faintest grey levels correspond to $\tau \sim 0.05$, a value commonly adopted as a threshold for line identification in high signal-to-noise spectra. Absorption saturates for $\tau \gtrsim 3$ ($e^{-\tau} \lesssim 0.05$).

As expected, these maps show stronger HeII absorption than HI absorption. HeII produces a substantial optical depth in regions that are nearly devoid of HI absorption, so HeII measurements can probe low density structure that is virtually undetectable by other means. Conversely, most regions with a significant HI optical depth produce saturated HeII absorption. The sharp edges visible in some of the saturated HeII features and the "blobbiness" of the weak HeII absorption are probably artifacts of representing the gas distribution with a discrete set of particles.

For quantitative analyses, we create simulated absorption spectra along random lines of sight through the simulation cube. Knowing the temperature and density of each SPH particle, we can compute the associated fractions of HI, HeI, and HeII given our assumed UV background. From these we compute the optical depths as a function of frequency by performing a line integral through the smoothing kernels of all SPH particles whose kernels intersect the line of sight, taking into account Hubble flow, peculiar velocities, and the thermal broadening appropriate to each of the absorbing species in order to transform from physical space to frequency space. Details of this procedure are described in HKWM.

3.1. Mean absorption and evolution with redshift

Figure 3a shows the redshift evolution of the effective mean optical depth for HeII absorption, $\overline{\tau}_{\rm HeII} \equiv -\log_e\langle F\rangle$, where F is the transmitted flux (with $F = 1$ corresponding to complete transmission). The average is performed over 100 lines of sight at each of the five output times. Because of the non-linear dependence of flux on optical depth, $\overline{\tau}_{\rm HeII}$ is not the mean value of $\tau_{\rm HeII}$ along the spectrum, but while $\langle F\rangle$ can be measured from a spectrum of imperfect resolution and finite signal-to-noise ratio, the mean value of $\tau_{\rm HeII}$ cannot. Thin lines show results for the three models with the UV background employed during dynamical evolution of the simulation, i.e., the HM background divided by a factor of two. The intensity of this UV background at energies responsible for ionizing HeII is approximately constant over the redshift range plotted here, though it does start to decline smoothly above $z \sim 3.5$. The mean optical depth decreases towards lower redshift primarily because the expansion of the universe reduces the HeII fraction, since it lowers the physical density of the absorbing medium and hence the recombination rate per HeIII ion. Cosmic expansion also spreads the atoms in a given comoving region over a larger range in frequency. These are precisely the effects that determine the evolution of the Gunn-Peterson

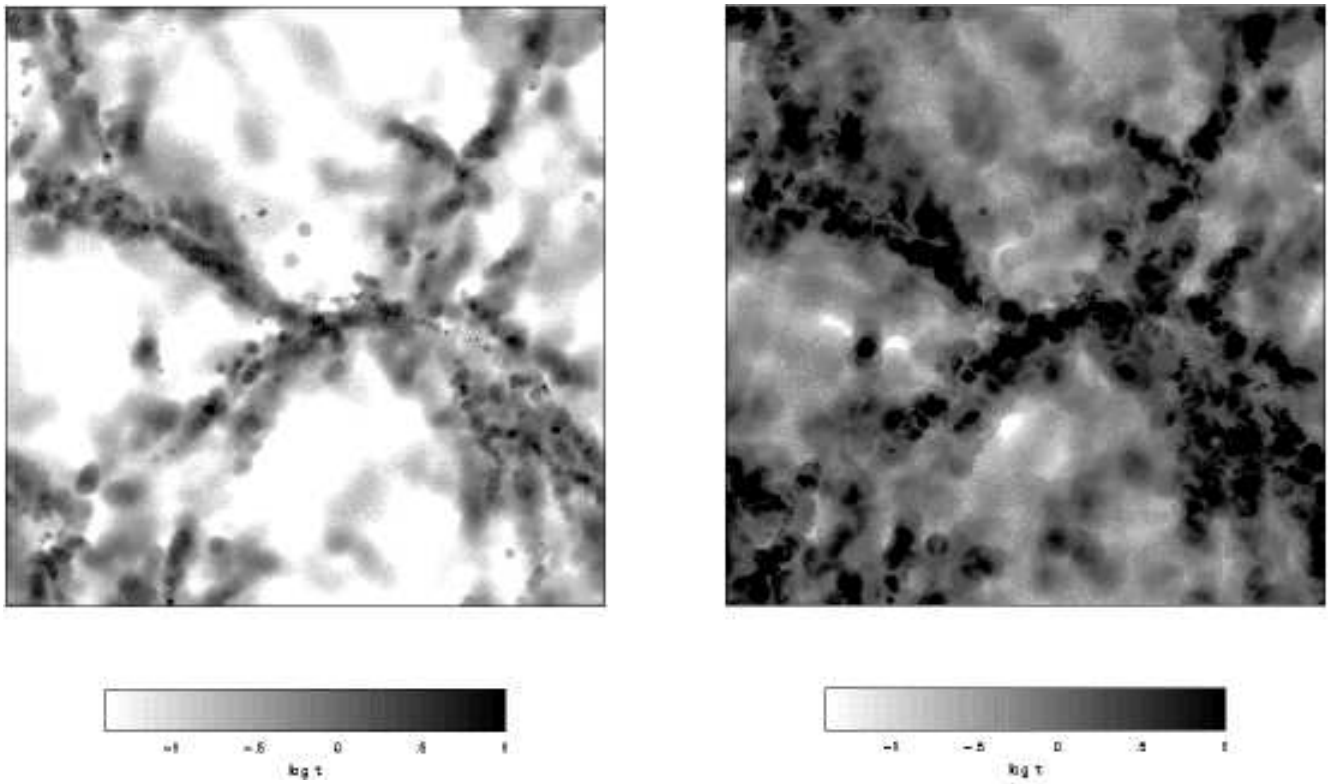

Fig. 2.— Optical depth to HI (left) and HeII (right) absorption in the SCDM simulation at $z = 2.33$. The optical depth is averaged over a slice of velocity width 60 $\mathrm{km\,s^{-1}}$ through the middle of the simulation cube. The scale is logarithmic in τ, as indicated, with the faintest grey levels corresponding to $\tau \sim 0.05$. The intensity of the UV background has been scaled so that the simulation produces the mean HeII opacity measured by DKZ (see discussion in §3.1). HeII absorption is prominent in low density regions that are nearly transparent in HI.

optical depth produced by a uniform IGM with a constant UV background. The first effect, which dominates here, would not apply to gas in collapsed, physically stable structures. While Figure 2 shows that the absorption is by no means uniform, the rapid evolution of $\overline{\tau}_{\rm HeII}$ is a strong hint that the absorbing gas resides in low density structures that are still expanding with the cosmic background.

The solid triangle in Figure 3a shows HAR's observational estimate, $\overline{\tau}_{\rm HeII} = 2.0^{+1.0}_{-0.5}$ (2σ errors) at $z = 3.3$, measured outside the ionization zone produced by the observed quasar. The wavelength range contributing to this point is about $40\mathring{A}$. Solid circles with error bars show $\overline{\tau}_{\rm HeII}$ at lower redshifts from the DKZ spectrum. Each point corresponds to a single $10\mathring{A}$ bin from DKZ's figure 1 — we measured the extrapolated quasar continuum and observed flux from this figure and divided them to obtain $F = \exp(-\overline{\tau}_{\rm HeII})$. The error bars are 1σ and are based on the noise vector in DKZ's figure. The fluctuations from point to point are larger and more coherent than expected from observational errors alone. They are presumably caused by large scale density variations, or possibly by inhomogeneity in the background radiation field.

Comparison between the data points and the thin lines in Figure 3a shows that the CDM models produce roughly the correct trend of $\overline{\tau}_{\rm HeII}$ with redshift but have an overall level of absorption that is too low. The intensity of the ionizing background used during the dynamical evolution of the simulations is already a factor of two lower than that advocated by HM, but a further reduction is necessary to match the observed mean absorption. To quantitatively compare the models, we calculate the factor

$$C_{\rm HeII} = \frac{{}_{\rm HM}\Gamma_{\rm HeII}}{{}_{\rm req}\Gamma_{\rm HeII}}, \tag{7}$$

where ${}_{\rm req}\Gamma_{\rm HeII}$ is the photoionization rate required to match the observed HeII optical depth and ${}_{\rm HM}\Gamma_{\rm HeII}$ is the photoionization rate predicted by the HM background (equations 3 and 4). Changing the intensity of the UV background within a broad range does not significantly alter the temperatures or spatial distribution of the absorbing gas, so we are able to estimate ${}_{\rm req}\Gamma_{\rm HeII}$ by rescaling the background after the simulation has been run but before creating simulated spectra (see Miralda-Escudé et al., in preparation, for numerical tests of this scaling). In fact, because photoionization completely dominates over collisional ionization in the absorbing regions, we could obtain virtually identical results by the still simpler procedure of rescaling optical depths in the extracted spectra.

The HeII absorption value we match is the quoted value of $\overline{\tau}_{\rm HeII} = 1.0 \pm 0.07$ at $z = 2.4$ from DKZ. We find $C_{\rm HeII}$ by an iterative interpolation search, dividing the HM ionization parameters by different factors until we obtain the correct mean absorption. As we do not have a simulation output at $z = 2.4$, we linearly interpolate $\overline{\tau}_{\rm HeII}$ between $z = 2.33$ and $z = 2.67$. The values of $C_{\rm HeII}$ for the three cosmological models are listed in column 6 of Table 1. These factors are equal for the two low amplitude models, OCDM and SCDM. The required value for the CCDM model is much higher. This model tends to produce less absorption at fixed Γ because (as we will show in detail later) most of the flux decrement arises in large volumes that are near or below the mean

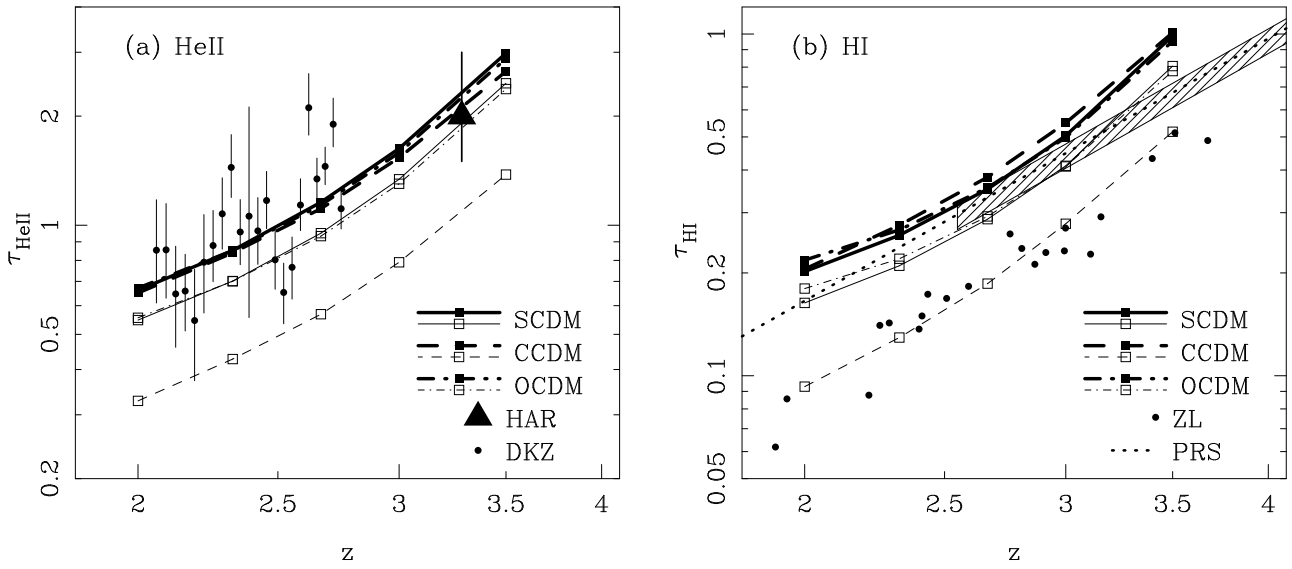

Fig. 3.— *(a)* Redshift evolution of $\overline{\tau}_{\rm HeII}$, the effective mean optical depth of HeII absorption. The horizontal axis (redshift) is scaled logarithmically in $(1+z)$, so that power-law relations between τ and $(1+z)$ would appear as straight lines. Thin lines with open squares show the results for the three CDM simulations calculated with the ionizing background intensity used during dynamical evolution. Thick lines with filled squares show $\overline{\tau}_{\rm HeII}$ after the intensity of the background is reduced by a factor of 1.5 for SCDM and OCDM and by 4.0 for CCDM. With this lower intensity, the simulations reproduce the mean optical depth measured by DKZ, $\overline{\tau}_{\rm HeII} = 1.0$ at $z = 2.4$. Points from the individual 10$\mathring{A}$ bins of the DKZ spectrum are shown as solid dots with 1σ error bars. The triangle shows the measurement and 2σ error bar of HAR, $\overline{\tau}_{\rm HeII} = 2.0^{+1.0}_{-0.5}$ at $z \approx 3.3$. *(b)* Same as *(a)*, but for HI absorption. Thin lines again correspond to the UV background used during dynamical evolution and thick lines to the background reduced by a factor of 1.5 (SCDM, OCDM) or 4.0 (CCDM). The dotted line is PRS's fit to the observed evolution of $\overline{\tau}_{\rm HI}$, which was calculated from data in the redshift range indicated by the hatched region. The vertical extent of this region illustrates the approximate 1σ confidence interval for the fit. The solid points are the measurements of mean optical depth from ZL for their "sample 2" quasars.

density. At the higher mass fluctuation amplitude of CCDM, more of the gas has flowed out of these void-like regions into higher density zones and collapsed objects; the absorption from these regions is already saturated, so adding more gas to them does not increase the mean decrement.

The heavy lines in Figure 3a show $\overline{\tau}_{\rm HeII}$ with the rescaled ionization parameters. A single value of $C_{\rm HeII}$ allows the models to fit the observed $\overline{\tau}_{\rm HeII}$ results at all redshifts from $z = 2$ to $z = 3.3$, to within the scatter of the data points, indicating that the evolution predicted by the simulations is consistent with the observations if the UV background evolves as predicted by HM. Although $\Gamma_{\rm HeII}$ falls by only 20% between $z = 2.4$ and $z = 3.3$, the models reproduce the factor of two difference between the DKZ and HAR measurements of $\overline{\tau}_{\rm HeII}$ because of the cosmic expansion effects discussed earlier.

Figure 3b shows the effective mean optical depth of HI absorption, $\overline{\tau}_{\rm HI} \equiv -\log_e\langle F_{\rm HI}\rangle$, for the three CDM models. Thin lines correspond to the UV background intensity adopted in the simulations, i.e., half of the HM background intensity at the corresponding redshift. Thick lines show $\overline{\tau}_{\rm HI}$ with the UV background intensity rescaled in order to match the observed $\overline{\tau}_{\rm HeII}$, i.e., the HM background (equations 3 and 4) divided at all redshifts by the factor $C_{\rm HeII}$ listed in Table 1.

The straight dotted line in Figure 3b shows the power-law fit $\overline{\tau}_{\rm HI} = 0.0037(1+z)^{3.46}$ found by Press, Rybicki, & Schneider (1993, hereafter PRS) in their analysis of the mean flux decrement in a sample of 29 high-redshift quasars. The hatched box shows the redshift extent of points used to compute this fit and the 1σ statistical uncertainty in the fit. PRS computed the mean decrement by extrapolating the quasar continuum from the region redward of Lyα emission into the Lyα forest region. Zuo & Lu (1993, hereafter ZL) estimated the mean decrement from higher resolution spectra by directly fitting the continuum to the regions of lowest absorption in the forest. We indicate their results by the filled circles in Figure 3b. Clearly the two observational determinations disagree by far more than their statistical uncertainties. A recent analysis of Keck HIRES spectra, using an approach similar to ZL's but data of higher resolution and signal-to-noise ratio, yields mean decrements that are much closer to the PRS values than to ZL's (Rauch et al. 1997). We will therefore proceed on the assumption that the PRS determination is accurate, but the systematic uncertainty in existing estimates of $\overline{\tau}_{\rm HI}$ is worth keeping in mind, as a major change to these estimates would affect our conclusions about the shape of the UV background spectrum.

Once the background intensity has been divided by the factor $C_{\rm HeII}$, the effective HI optical depths agree fairly well with the PRS determination, though they tend to rise above it at the low and high ends of our redshift range. To better quantify this agreement, we list in columns 7 and 8 of Table 1 the scaling factors $C_{\rm HI}$ (defined analogously to $C_{\rm HeII}$) by which the HM background must be divided in order that the simulation match the PRS optical depths at $z = 2$ and $z = 3$. These factors match the corresponding values of $C_{\rm HeII}$ to 20% or better in most cases (30% for CCDM at $z = 2$), indicating that the cosmological simulations and the HM spectral shape are, taken together, consistent with the joint observational constraints of DKZ and PRS. The HI scaling factors at $z = 2$ and $z = 3$ are also similar, indicating that the simulations reproduce the

PRS evolution law over this redshift range if the UV background evolves as predicted by HM. If this analysis is extended to $z \sim 4$, however, the simulations require a roughly constant $\Gamma_{\rm HI}$ (HKWM; Rauch et al. 1997), while the HM model predicts a substantial drop in $\Gamma_{\rm HI}$ towards high redshift because of the declining number density of quasar sources.

The uncertainty on the correct value of $C_{\rm HeII}$ is mainly statistical, and is dominated by the fact that an observational measurement of $\overline{\tau}_{\rm HeII}$ is only available from one QSO. The theoretical estimates at z=2.33 come from 200 lines of sight through the simulation box, which together cover a redshift patch equal to ~ 13 times the useful length of the DKZ spectrum. We can estimate the error in $C_{\rm HeII}$ by picking groups of simulated spectra with the same total length as DKZ from our ensemble of 200. We then calculate the $C_{\rm HeII}$ required to match the observational $\overline{\tau}_{\rm HeII}$ for each set of spectra. From the spread of $C_{\rm HeII}$ values we estimate the 1σ uncertainties on $C_{\rm HeII}$ to be $+10\%, -25\%$. The error in $C_{\rm HI}$ is dominated by systematic uncertainties in the observational determination of $\overline{\tau}_{\rm HI}$, probably associated with continuum fitting (see Rauch et al. 1997).

JBDGJP suggested that the high HeII optical depth towards Q0302-003 might arise because the HeII "Stromgren spheres" around quasars had not overlapped by $z = 3.3$, leaving most of the universe optically thick to HeII ionizing photons. Supporting evidence for this scenario comes from a rapid change at $z \sim 3.1$ in the SiIV/CIV ratios measured in Lyα absorbers, which suggests a change in the shape of the UV background spectrum that could correspond to percolation of quasars' HeII ionization zones (Songaila & Cowie 1996, but see also Hellsten et al 1997). Our results show that, in the CDM models, no major change in the spectral shape is needed to explain the existing HeII data. Indeed, if HAR's upper limit on $\overline{\tau}_{\rm HeII}$ is taken at face value, then the background spectrum cannot be much softer than the HM spectrum at $z = 3.3$, at least along this line of sight. If HAR's residual flux is an artifact of imperfect background subtraction, then our models could also accommodate HeII reionization at $z < 3.3$.

3.2. Implications for Ω_b

All of our models require $C_{\rm HI} \gtrsim 2.5$ to match the PRS determination of $\overline{\tau}_{\rm HI}$ and $C_{\rm HeII} \gtrsim 3$ to match the DKZ determination of $\overline{\tau}_{\rm HeII}$. If we had obtained values of $C_{\rm HI}$ and $C_{\rm HeII}$ smaller than unity from the simulations, we could accommodate them easily by appealing to additional UV sources not considered by HM, e.g., star-forming galaxies or faint AGNs. However, since the HM background is based on the observed population of quasar sources (with a modest extrapolation for quasars below existing survey detection limits), it is difficult to see how the true background could be lower than the HM background by such large factors. Reductions of this magnitude would also make the background intensity inconsistent with estimates from the proximity effect (Giallongo et al. 1996 and references therein), though these are subject to significant systematic uncertainties. Even allowing for the imperfect resolution of the simulations and plausible uncertainties in the background intensity, it seems that these cosmological models for the Lyα forest are at best marginally compatible with the PRS opacity measurements if $\Omega_b h^2 = 0.0125$.

The alternative to lowering the UV background is to raise the mean baryon density. The Lyα optical depth is proportional to the number density of absorbing atoms (see equation [6]), which for highly photoionized gas is proportional to the square of the gas density divided by the photoionization rate. The second power of density arises because the the recombination rates per HII or HeIII ion are themselves proportional to the density. If the distribution of *over*densities ($\rho_b/\bar{\rho}_b$) and gas temperatures in the IGM is unchanged by altering Ω_b, then the optical depth τ at a specified redshift along a line of sight is proportional to Ω_b^2/Γ. Note that the effective mean optical depth $\overline{\tau}$ is not simply proportional to Ω_b^2/Γ because of the non-linear nature of flux averaging, but it is still the case that raising Ω_b by a factor $C^{1/2}$ should have the same effect as lowering Γ by a factor C. The assumption that the absorbing gas is highly photoionized breaks down in regions that are collisionally ionized (e.g., hot gas in virialized halos) or predominantly neutral (e.g, damped Lyα systems), but these are too rare to make much contribution to $\overline{\tau}$.

We have completed one simulation of the SCDM model with $\Omega_b = 0.125$ instead of 0.05, and we find that the scaling of τ with Ω_b is weaker than the above argument would suggest, roughly $\tau \propto \Omega_b^{1.7}$ instead of $\tau \propto \Omega_b^2$. The reason is that raising Ω_b also raises the gas temperature in the low and moderate density regions ($\rho_b/\bar{\rho}_b \lesssim 10$) that produce most of the absorption, because increasing the HI and HeII fractions allows a given volume of gas to absorb energy from the photoionizing background at a higher rate. Since the recombination rates decline as $T^{-0.7}$ in the relevant temperature regime, the HI and HeII fractions do not rise by the full Ω_b^2 factor when Ω_b is increased. The physics of the Ω_b scaling does not depend on the cosmological scenario, and we therefore expect the result derived from our pair of SCDM simulations to hold more generally (but see the discussion of reionization effects at the end of §3.4). One might think that reducing Γ at fixed Ω_b would also alter the gas temperatures, but it does not, because the increase in HI and HeII fractions is exactly compensated by the smaller rate of photoionizations per ion. The scaling $\tau \propto \Gamma^{-1}$ is therefore preserved unless the *shape* of the ionizing background, which determines the mean residual energy per photoelectron, is altered.

With these scalings in mind, we can relate the values of $C_{\rm HI}$ and $C_{\rm HeII}$ listed in Table 1 to the combination of Γ, Ω_b, and h that is required for the simulation to match the observed mean opacity:

$$C = \left(\frac{\Gamma_{\rm HM}}{\Gamma_{\rm true}}\right)\left(\frac{\Omega_b h^2}{0.0125}\right)^{1.7}\left(\frac{h_{\rm sim}}{h}\right), \qquad (8)$$

where $h_{\rm sim}$ is the value of h adopted in the simulation. The h dependences arise because the mean gas density is proportional to h^2 at fixed Ω_b and because the optical depth at fixed HI or HeII density is inversely proportional to the Hubble constant (equation [6]). If we assume that $\Gamma_{\rm true} = \Gamma_{\rm HM}$ and $h = h_{\rm sim}$, then matching the PRS values of $\overline{\tau}_{\rm HI}$ requires $\Omega_b h^2 \sim 0.023$ for SCDM and OCDM and $\Omega_b h^2 \sim 0.038$ for CCDM. Matching the DKZ measurement of $\overline{\tau}_{\rm HeII}$ requires a similar baryon density, though the HeII opacity on its own gives a less compelling argument for high Ω_b because the lower limit on $\Gamma_{\rm HeII}$ is less secure than the lower limit on $\Gamma_{\rm HI}$. Assuming standard big bang nucleosynthesis, a density $\Omega_b h^2 = 0.023$ is in excellent agreement with Tytler

et al.'s (1996) estimate of the primordial deuterium abundance, but it is inconsistent with the much higher deuterium abundances estimated by Carswell et al. (1994), Songaila et al. (1994), and Rugers & Hogan (1996ab). We examine the baryon density required by cosmological simulations of the Lyα forest more thoroughly in Rauch et al. (1997), which includes a new determination of $\overline{\tau}_{\rm HI}(z)$ from high resolution spectra and a discussion of the lower limit on $\Gamma_{\rm HI}$. The analytic arguments presented in Weinberg et al. (1997) show that the lower limits on Ω_b derived from this method depend only on very general properties of the "cosmological" picture of the Lyα forest, and are unlikely to be weakened substantially by changes in the adopted cosmological model or the numerical resolution of the simulations.

3.3. Simulated HeII spectra

The top panels of Figure 4 show examples of HI (solid lines), HeI (dotted lines), and HeII (dashed lines) absorption along two randomly selected lines of sight through the SCDM simulation, at $z = 2.33$. We have scaled the HM ionizing background by the factor $C_{\rm HeII}$ listed in Table 1, so that the mean optical depth matches the DKZ observation. The transmission $e^{-\tau}$ is plotted against line-of-sight velocity. The corresponding baryon density (in units of the mean baryon density) is plotted below each spectrum in the second panel, with the solid line showing the redshift space density and the dotted line the real space density (i.e., the density computed with peculiar velocities and thermal broadening set to zero). The HI optical depth is well correlated with the redshift space density. Features in the redshift space density field are usually offset from those in the real space field because of peculiar motions, and the high density peak in the left hand spectrum is greatly broadened in redshift space because of infall. HeI absorption is non-negligible only in the highest density region of the second spectrum, where the high recombination rate increases the relative fraction of neutral helium. HeII absorption, on the other hand, is quite strong, and most of it arises in regions where the HI optical depth is quite low. The ratio $\tau_{\rm HeII}/\tau_{\rm HI}$ (shown by the solid line in the third panel) is about a factor of eight over most of the spectrum. The HI and HeII flux decrements, $1 - e^{-\tau}$, are nearly equal when the HI optical depth is high, but when $\tau_{\rm HI}$ is small the HeII flux decrement is eight times higher. HeII absorption therefore probes regions of lower density than HI absorption, as already seen in Figure 2.

The optical depth ratio $\tau_{\rm HeII}/\tau_{\rm HI}$ is high and approximately constant, as anticipated by Miralda-Escudé (1993). Variations arise when collisional ionization or thermal broadening of the spectrum become important — these processes affect HeII and HI differently because of the differences in ionization potential and atomic mass, respectively. The dotted line in the third panel of Figure 4 shows the optical depth ratio calculated from spectra along the same lines of sight with no thermal broadening applied. The variations seen in the solid line largely disappear, indicating that thermal broadening is their primary cause, at least along these two lines of sight.

For a more quantitative view of the optical depth ratio, we examine the joint distribution of $\tau_{\rm HeII}$ and $\tau_{\rm HI}$ in 200 spectra extracted along random lines of sight through the SCDM simulation

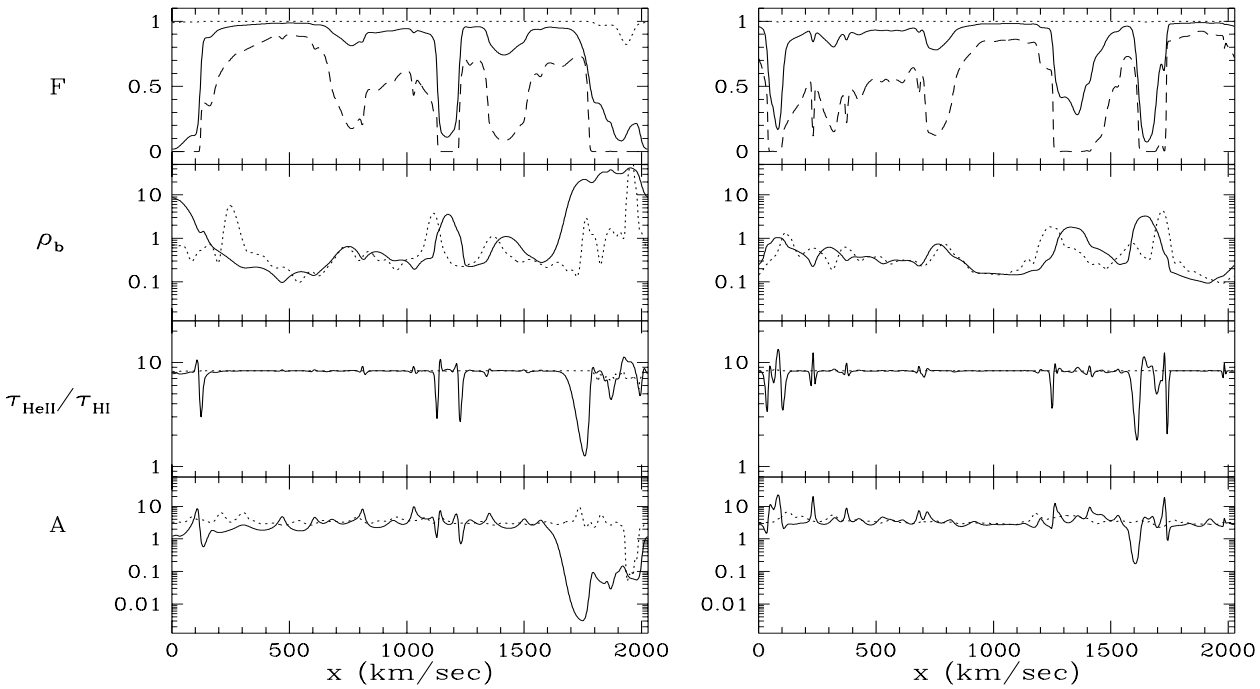

Fig. 4.— Two examples of spectra taken along random lines of sight through the simulation box of the SCDM model, at a redshift $z = 2.33$. The top panel shows transmitted flux against line-of-sight velocity for HI (solid line), HeI (dotted line), and HeII (dashed line). The second panel shows the density of baryonic matter, in units of the mean baryon density, in redshift space (solid line) and real space (dotted line). The third panel shows the ratio $\tau_{\rm HeII}/\tau_{\rm HI}$ computed with (solid line) and without (dotted line) thermal broadening of the absorption. The bottom panel shows the ratio $A = \tau_{\rm HeII}/\rho_b^{1.6}$ computed in redshift space (solid line) and real space (dotted line).

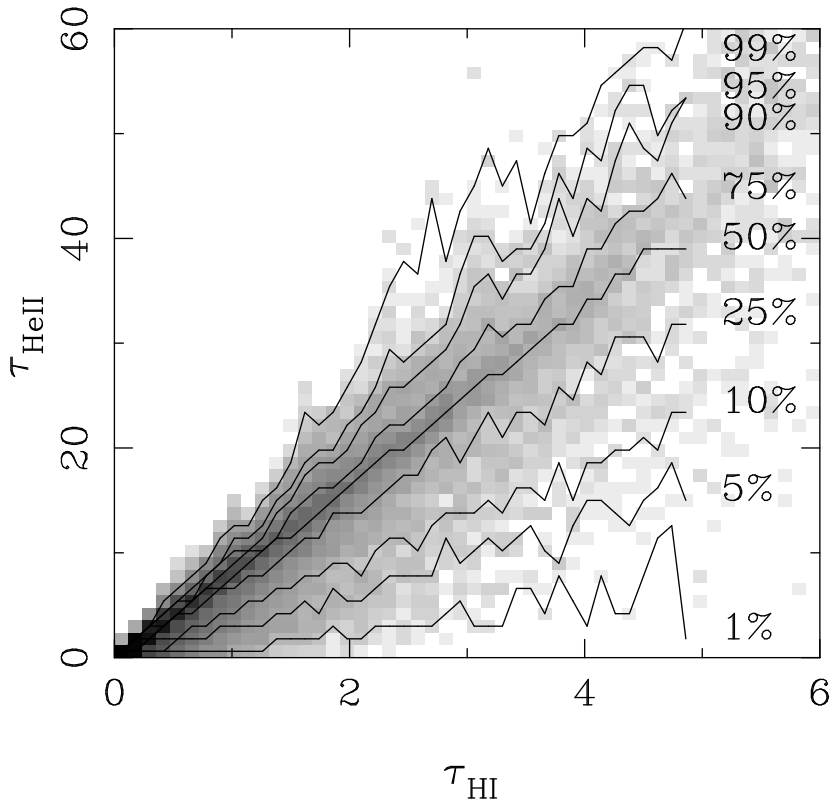

Fig. 5.— The joint distribution of $\tau_{\rm HeII}$ and $\tau_{\rm HI}$ in the SCDM model at $z = 2.33$, computed from 200 spectra, each with 1000 pixels. The logarithmic grey scale shows the fraction of pixels in bins of $\Delta\tau_{\rm HI} = 0.12$, $\Delta\tau_{\rm HeII} = 1.2$. Lines show the percentile distribution of $\tau_{\rm HeII}$ in each bin of $\tau_{\rm HI}$.

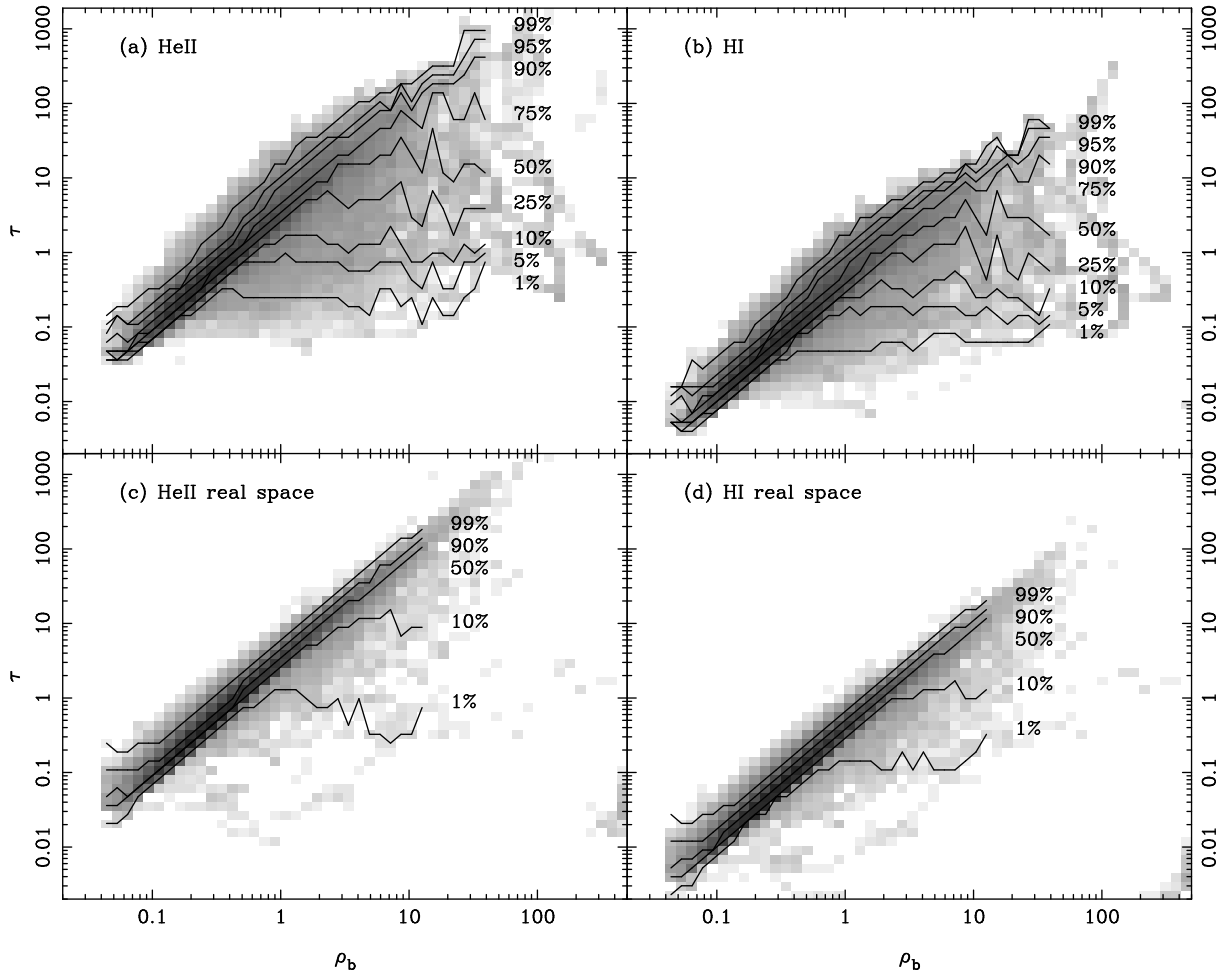

Fig. 6.— The joint distribution of optical depth and ρ_b (in units of the mean baryon density) for the SCDM model at $z = 2.33$, in a format similar to Fig. 5. *(a)* HeII in redshift space. *(b)* HI in redshift space. *(c)* HeII in real space. *(d)* HI in real space.

at $z = 2.33$. The logarithmic grey scale in Figure 5 indicates the distribution of pixels in the $\tau_{\rm HI} - \tau_{\rm HeII}$ plane. There are 2×10^5 pixels in total, 1000 in each of the 200 spectra. The labeled lines in Figure 5 show the percentile ranges of $\tau_{\rm HeII}$ in bins of $\Delta\tau_{\rm HI} = 0.12$, i.e., of the pixels that have a given value of $\tau_{\rm HI}$, 1% have $\tau_{\rm HeII}$ below the 1% line, 5% below the 5% line, and so forth. Most pixels lie along a well defined ridge at $\tau_{\rm HeII} = 8\tau_{\rm HI}$, tracked by the median $\tau_{\rm HeII}$ line. Collisional ionization in shock heated regions raises $\tau_{\rm HeII}/\tau_{\rm HI}$ because it suppresses HI absorption more strongly than HeII absorption. Thermal broadening on the edges of high density regions tends to reduce $\tau_{\rm HeII}/\tau_{\rm HI}$ by spreading HI absorption into the lower density surroundings. Both effects can be seen in Figure 5, but the scatter below the median relation is broader than the scatter above it, confirming the anecdotal evidence of Figure 4 that thermal broadening is the dominant cause of variations in $\tau_{\rm HeII}/\tau_{\rm HI}$.

Most of the absorbing gas in Figure 4 has relative density $\rho/\bar{\rho}$ between 0.1 and 10. In these simulations, the gas in this density regime typically follows a tight and simple relation between temperature and density, approximately $T \propto \rho^{0.6}$ (see figure 3b of Weinberg, Hernquist & Katz 1997). This relation arises because the gas is cooled by adiabatic cooling and heated by photoionization, at a rate that depends on the density. Changing the gas temperature alters the heating rate, and gas that lies off this relation evolves towards it on a Hubble timescale (for a more detailed discussion see Hui & Gnedin 1996). The relation breaks down in collapsed regions, where shock heating and radiative cooling become important. The optical depth to HI or HeII Lyα absorption is proportional to the number density of HI or HeII atoms at the corresponding line-of-sight velocity. These are proportional to the gas density multiplied by the recombination rate, which is in turn proportional to $\rho T^{-0.7}$ for temperatures up to several $\times\, 10^4$ K. Gas that lies on the $T \propto \rho^{0.6}$ temperature-density relation should therefore satisfy $\tau_{\rm HeII} \propto \rho^2 (\rho^{0.6})^{-0.7} \propto \rho^{1.6}$. The solid line in the bottom panel of Figure 4 plots the ratio $A = \tau_{\rm HeII}/\rho^{1.6}$ against velocity, and it is indeed approximately constant over most of the spectrum. The variations are caused primarily by peculiar velocity distortions of the redshift space density, since it is the real space density that is directly correlated with the temperature. In real space (dotted line) the variations are much smaller, with the one major departure occurring in the high density region of the left hand spectrum, where shock heating drives the gas off the simple temperature-density relation. Figure 6a shows the joint distribution of $\tau_{\rm HeII}$ and ρ, in redshift space, for the 200 spectra examined in Figure 5. Most pixels lie on the ridge $\tau_{\rm HeII} \approx 3.5(\rho/\bar{\rho})^{1.6}$, though there is a scatter towards lower $\tau_{\rm HeII}$ at higher densities because of shock heating. The joint distribution of $\tau_{\rm HI}$ and ρ (Figure 6b) is similar, except for a factor of eight offset. The factor of two interquartile scatter at low densities in these plots is caused predominantly by peculiar velocity effects, as one can see from the corresponding real space joint distributions (Figures 6c and 6d).

To a first approximation, one can thus regard a HeII or HI absorption spectrum as a map of the gas density field along the line of sight, albeit a map that is non-linear (an exponential of a power-law) and distorted by peculiar velocities. Figures 4–6 use the SCDM model for illustration, but the qualitative physical picture is similar in all three of the cosmological scenarios that we

consider. This picture can be contrasted with a traditional phenomenological description of the Lyα forest as a collection of discrete absorbing clouds, each producing a Voigt-profile line fully characterized by a redshift, an HI column density, and a b-parameter (velocity width). One can compute the HeII absorption produced by "line blanketing" in such a model by assuming a ratio $n_{\rm HeII}/n_{\rm HI}$ and either thermal broadening (in which case the HeII b-parameters are a factor of two smaller than the HI b-parameters) or "turbulent" broadening (in which case the b-parameters are equal). For a heavily saturated but undamped line, the equivalent width is proportional to the b-parameter.

In order to compare the simulation results to this sort of discrete cloud model, we have used a program written by J. Miralda-Escudé to generate artificial spectra that are superpositions of randomly distributed, Voigt-profile lines. We draw HI column densities from a power-law distribution, $dN/dN_{\rm HI} \propto N_{\rm HI}^{-1.5}$, with a lower cutoff at $N_{\rm HI,min} = 10^{12}$ cm^{-2}, and b-parameters from a Gaussian distribution with a mean of 28 km s^{-1} and a dispersion of 10 km s^{-1}, truncated below $b_{\rm min} = 18$ km s^{-1}. These parameters, based on Hu et al. (1995), are similar to those used by Songaila et al. (1995) in their modeling of the JBDGJP observation, though we have lowered $N_{\rm HI,min}$ from 2×10^{12} cm^{-2} to 10^{12} cm^{-2}. We choose the mean number of lines per unit redshift in order to match the PRS determination of $\overline{\tau}_{\rm HI}$ at $z = 2.33$. We then generate two sets of corresponding HeII spectra, one for pure thermal broadening, one for pure turbulent broadening, choosing the $n_{\rm HeII}/n_{\rm HI}$ ratio in each case to reproduce the DKZ value of $\overline{\tau}_{\rm HeII}$ at $z = 2.33$.

Figure 7 shows two examples of the line model spectra. Comparing to Figure 4, we see that while the HI spectra look qualitatively similar to those produced by the cosmological simulations, the HeII spectra look quite different — they are sharply corrugated, with many saturated regions in each spectrum. The simulations reproduce the observed values of $\overline{\tau}_{\rm HI}$ and $\overline{\tau}_{\rm HeII}$ at $z = 2.33$ simultaneously if $\Gamma_{\rm HI}/\Gamma_{\rm HeII} \approx 100$, as implied by the HM background spectrum. Our line models reproduce $\overline{\tau}_{\rm HI}$ and $\overline{\tau}_{\rm HeII}$ by construction, but the required UV background spectrum is much softer, with $\Gamma_{\rm HI}/\Gamma_{\rm HeII} \sim 200$ for the turbulently broadened model and ~ 2500 for the thermally broadened model. If the minimum column density is pushed far below 10^{12} cm^{-2}, then the qualitative properties of the line model become closer to those of the simulations, since the weak lines overlap to produce a fluctuating background that gives rise to much of the HeII absorption. Whether the underlying physical picture approaches that of the simulations depends on how one envisions the absorbers themselves. In a discrete cloud model, the absorption arises in physically distinct objects whose wings overlap in frequency space because of line broadening, but in the cosmological simulations the absorption arises in a smoothly fluctuating, continuous IGM.

3.4. Statistical analysis of transmission and optical depth

We now turn to statistical measures that quantify properties of the absorbing gas in the various models that we have introduced. These statistical predictions can be used to test and differentiate these models.

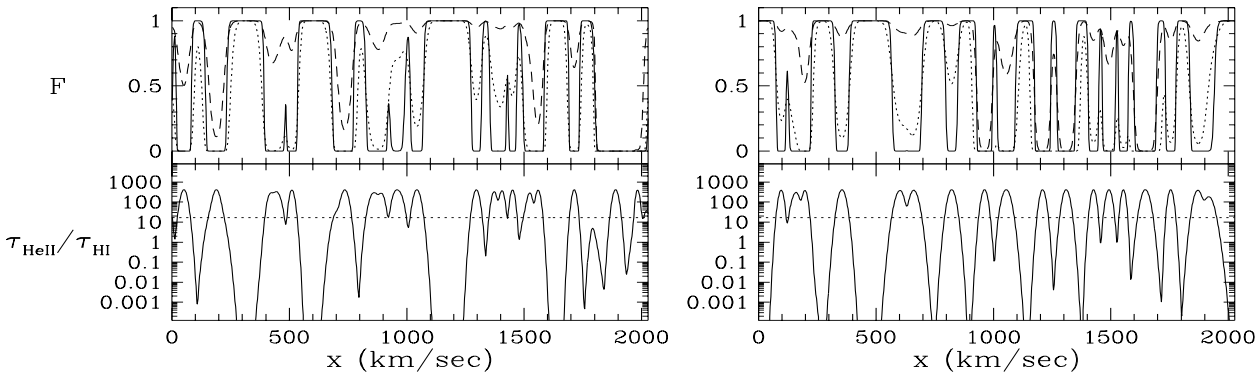

Fig. 7.— Two spectra generated from a model of randomly distributed, Voigt-profile lines. Dashed lines in the top panels show transmitted flux in the HI Lyα spectrum. Solid and dotted lines show HeII transmission assuming thermal broadening and turbulent broadening, respectively. The spectra are normalized to produce the observed values of $\overline{\tau}_{\rm HI}$ and $\overline{\tau}_{\rm HeII}$. The bottom panels show the ratio $\tau_{\rm HeII}/\tau_{\rm HI}$. This is constant for the turbulent broadening model (dotted line) because each line's HI and HeII b-parameters are identical. In the thermal broadening model (solid line), the ratio varies strongly because of the factor of 2 difference in b-parameters.

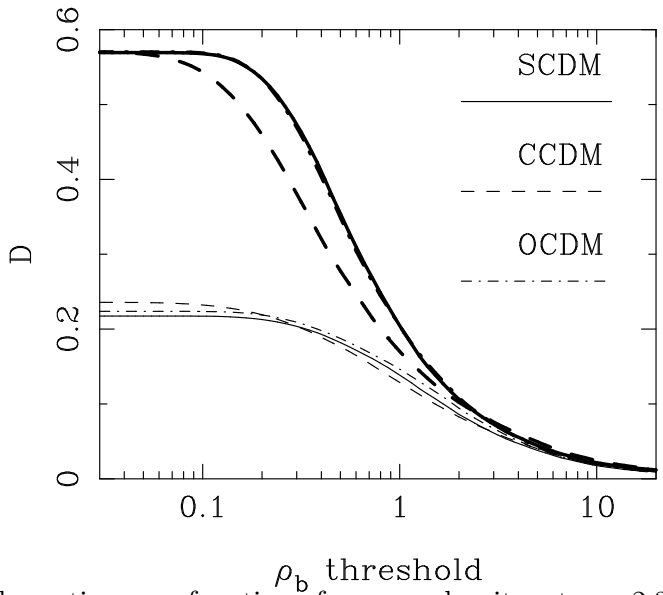

Fig. 8.— Mean absorption as a function of gas overdensity, at $z = 2.33$. $D = \langle 1 - F \rangle$ is the mean flux decrement in the spectrum after the contribution of gas with density below a threshold value of ρ_b (in units of the mean baryon density) is eliminated. Thick lines show results for HeII, thin lines for HI. The SCDM, CCDM, and OCDM models are represented by solid, dashed, and dot-dashed lines, respectively.

Figure 8 demonstrates a point suggested qualitatively earlier: most of the HeII absorption in the cosmological simulations arises in low density regions. We compute the mean flux decrement, $D = \langle 1 - F \rangle$, after setting to zero the absorption caused by gas with baryon density below a specified threshold. The flux decrement is plotted as function of the ρ_b threshold (in units of the mean baryon density). Regions with overdensity $\rho_b/\bar{\rho_b} < 2$ account for roughly 80% of the HeII flux decrement. This density regime should be amenable to approximate analytic treatments — though not necessarily to linear perturbation theory *per se* — so analytic methods like that of Reisenegger & Miralda-Escudé (1995; see numerical tests in Miralda-Escudé et al. 1996) should provide useful guides to the predictions of HeII absorption in CDM-like models. We see from Figure 8 that the SCDM and OCDM models, which have similar mass fluctuation amplitudes, produce their HeII absorption in almost identical density regimes. In the higher amplitude, CCDM model, noticeably less absorption arises in moderately underdense regions. As discussed in §3.1, more material in the CCDM model has flowed out of "voids" into relatively dense objects, which produce saturated HeII absorption. If the intensity of the UV background were held constant, this model would produce substantially less HeII absorption than the other two, as shown by the thin lines in Figure 3. We have rescaled the background intensity so that all three models produce the same mean absorption, but the greater emptiness of voids in the CCDM model remains evident in the density distribution of the absorbing material.

When the same analysis is applied to HI absorption (thin lines in Figure 8), we see a shift towards higher density regions. The density regime $\rho_b/\bar{\rho_b} < 2$ accounts for $\sim 55\%$ of the HI flux decrement, compared to 80% for HeII. Regions below the mean density produce $\sim 65\%$ of the HeII absorption but only $\sim 35\%$ of the HI absorption. Small differences between the models appear mainly because scaling the UV background to match $\overline{\tau}_{\rm HeII}$ does not give exactly the same $\overline{\tau}_{\rm HI}$ in each case.

The baryon density ρ_b is not directly observable, but it is well correlated with the HI optical depth, which is observable. The upper left panel of Figure 9 is analogous to Figure 8, except that we use a threshold in $\tau_{\rm HI}$ instead of a threshold in ρ_b, and we convert the mean flux decrement to an equivalent $\overline{\tau}$ in order to improve the dynamic range of the plot. We set the absorption of regions with $\tau_{\rm HI}$ below the threshold to zero before computing the mean decrement, D, and $\overline{\tau} = -\log_e(1 - D)$. At high values of $\tau_{\rm HI}$, the HI curves (thin lines) and HeII curves (thick lines) for each model converge, since saturated regions completely absorb both HI and HeII. However, much of the HeII absorption is associated with regions that have low HI optical depth. For example, half of the contribution to $\overline{\tau}_{\rm HeII}$ comes from regions with $\tau_{\rm HI} < 0.15$. Only $\sim 15\%$ of $\overline{\tau}_{\rm HI}$ is produced by these regions. Figure 2 demonstrates that low density regions are revealed more clearly by HeII absorption than by HI absorption. Figure 9 demonstrates that these regions are in fact responsible for much of the HeII opacity of the high redshift universe.

The upper right panel of Figure 9 compares the SCDM model to the two line models. The thermal and turbulent models are based on identical HI line populations, so their HI curves are identical, and their HeII curves are very similar. Even in the line models, much of the HeII

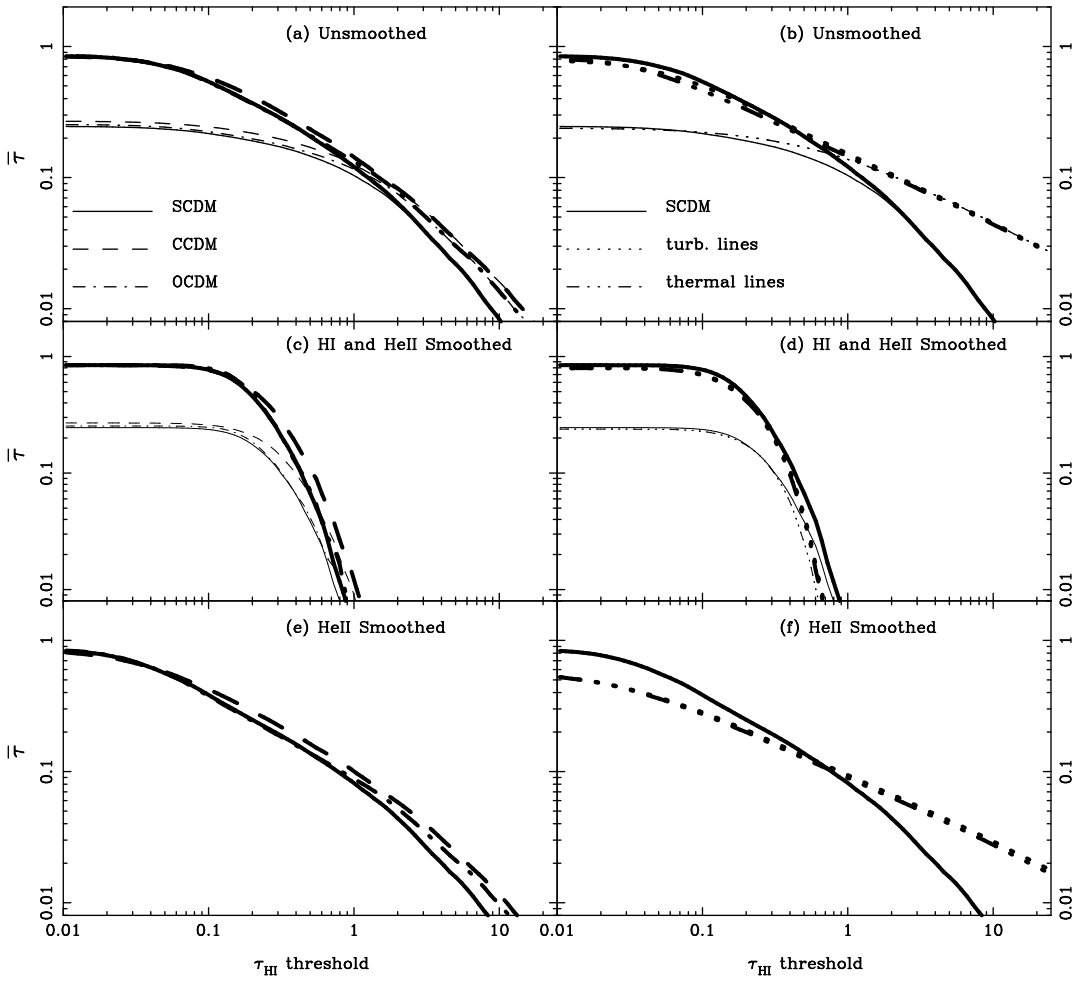

Fig. 9.— Effective mean optical depth as a function of $\tau_{\rm HI}$ threshold, at $z = 2.33$, analogous to Fig. 8. The value of $\overline{\tau} = -\log_e\langle F\rangle$ is calculated after setting $F = 1$ for points in the spectrum that have optical depth $\tau_{\rm HI}$ below the threshold value on the horizontal axis. Thick lines show $\overline{\tau}_{\rm HeII}$ and thin lines $\overline{\tau}_{\rm HI}$. Left hand panels compare the three CDM models; right hand panels compare the SCDM model to the line models with turbulent and thermal broadening. HI curves are identical for the two line models, since they assume identical HI line populations. Top panels show results for unsmoothed spectra. Middle panels show results after HeII and HI spectra are smoothed with a Gaussian filter of FWHM $\Delta v = 890$ km s^{-1}, corresponding to $3\mathring{A}$ in the HeII spectrum. Bottom panels show results when the HeII spectra are smoothed but the HI spectra are not. Only HeII curves appear in the bottom panels, since the HI curves would be identical to those in the top panels.

absorption occurs in regions of low HI optical depth — weak lines and the wings of strong lines. Relative to the CDM simulations, however, both line models produce a much larger fraction of $\overline{\tau}_{\rm HeII}$ in saturated regions. This difference corresponds to the visual impression one obtains by comparing sample spectra (Figures 4 and 7).

The DKZ data have a spectral resolution of approximately $3\mathring{A}$ (Gaussian FWHM), so the predictions in the top panels of Figure 9 cannot be compared directly to the DKZ observations. The middle panels show the same analysis after the model HI and HeII spectra have been convolved with a Gaussian filter of 890 km s^{-1} FWHM, equivalent to $3\mathring{A}$ for HeII at $z = 2.33$. Regrettably, this smoothing eliminates most of the difference between the CDM models and the line models. The sense of this difference is reversed relative to the full resolution case, with the CDM models producing a slightly larger fraction of their absorption at high values of (smoothed) $\tau_{\rm HI}$. This change probably reflects the large scale clustering that is present in the CDM models but not in the line models. Among the CDM models themselves, it is the more strongly clustered, CCDM model that produces the largest fraction of its absorption at high $\tau_{\rm HI}$.

The bottom panels of Figure 9 repeat the optical depth analysis using smoothed HeII spectra but unsmoothed HI spectra, in recognition of the fact that the best ground-based spectra are able to resolve even the narrowest observed HI Lyα features. This version of the analysis preserves the clear distinction between the CDM models and the line models visible in the upper panels. Indeed, smoothing the line models amplifies the difference between them and the CDM models, since a significant fraction of the line models' smoothed HeII flux decrement arises in "inter-line" regions where the HI optical depth is extremely low. While a realistic comparison to observations will have to contend with noise in the HeII and (to a lesser extent) HI data, the distinction between the line models and the CDM models is likely to be observable. The distinctions among the CDM models themselves are more subtle.

Figure 10 shows the distribution function of transmitted flux F; $P(F)dF$ is the probability that a randomly selected point in the spectrum has transmitted flux in the infinitesimal range $F \longrightarrow F + dF$. Thick and thin lines represent HeII and HI results, respectively. Left hand panels compare the three CDM models, and right hand panels compare the SCDM model to the line models. Upper panels are based on unsmoothed spectra, lower panels on spectra smoothed over 890 km s^{-1}. Figure 11 shows the distribution function of the log of the optical depth normalized so that $\int P(\log\tau))d\log(\tau) = 1$. While the information is equivalent in principle to that in Figure 10, the optical depth plot reveals tails of the distribution function more clearly.

The distribution functions of the three CDM models are rather similar, though they are somewhat broader for the CCDM model because of its higher clustering amplitude. At full resolution, the HeII distribution functions of the CDM models are radically different from those of the line models, especially at low optical depths ($F \approx 1$). The line models have gaps in their spectra where the HeII absorption is extremely low, but the CDM models do not. The resulting difference in $P(F)$ — an upturn at $F \approx 1$ for the line models but a downturn for the CDM

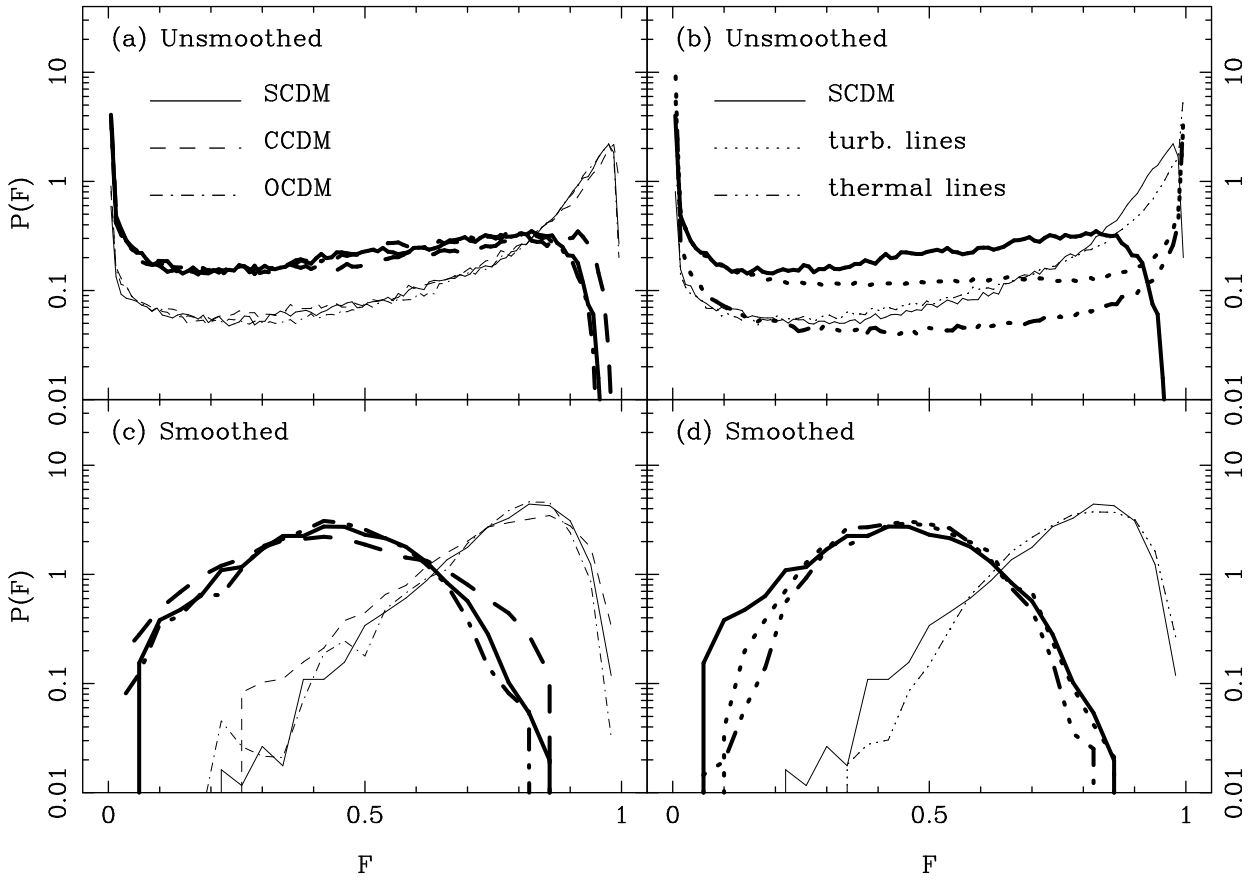

Fig. 10.— The distribution function of transmitted flux for z=2.33. $P(F)dF$ is the probability that a randomly selected point in the spectrum has transmitted flux in the range $F \longrightarrow F+dF$. As in Fig. 9, thick lines show HeII and thin lines HI, left hand panels compare the CDM models, and right hand panels compare SCDM to the two line models. Top panels show results for unsmoothed spectra. Bottom panels show results after the spectra are smoothed with a Gaussian of FWHM $\Delta v = 890$ km s^{-1}.

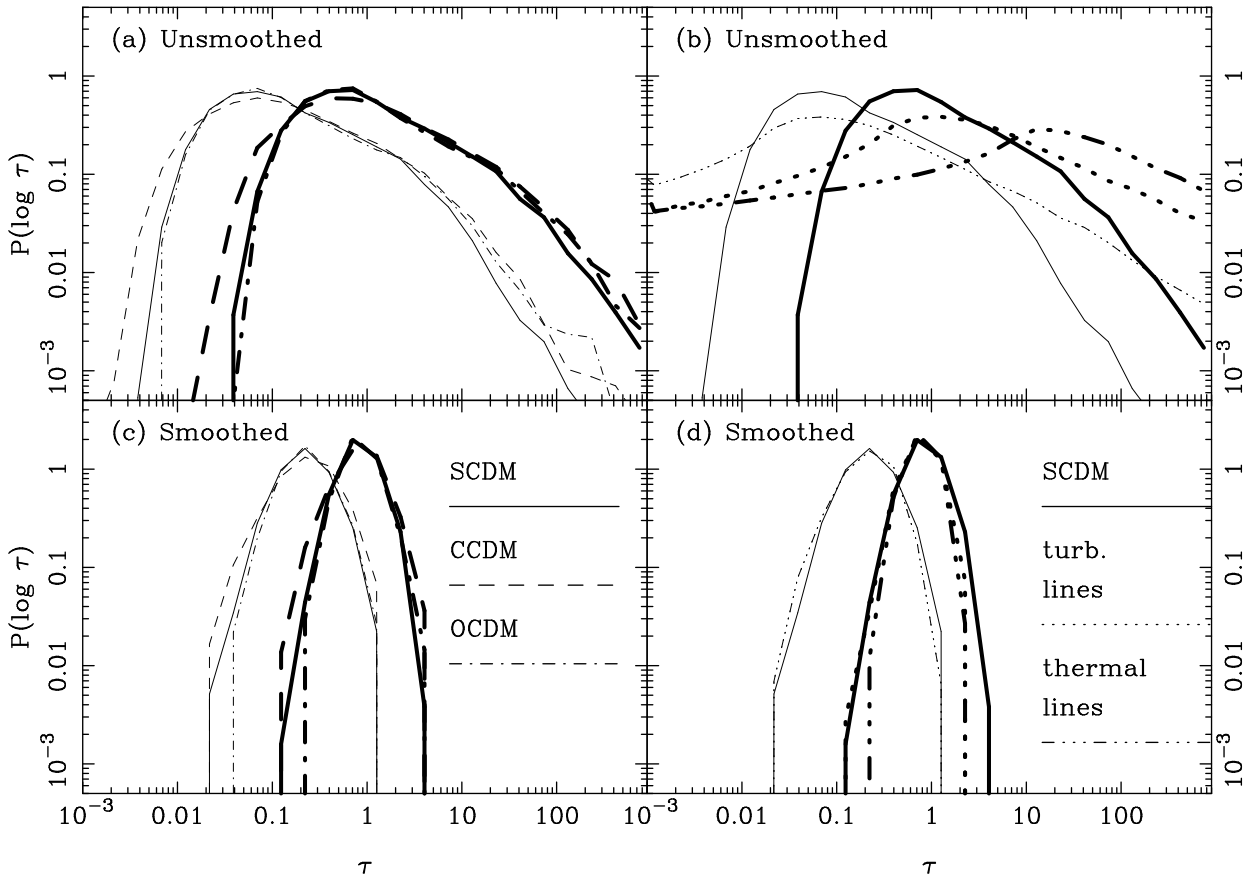

Fig. 11.— The distribution function of optical depth in logarithmic bins for z=2.33. $P(\log\tau)d\log\tau$ is the probability that a randomly selected point on the spectrum has the log of the optical depth in the range $\log\tau \longrightarrow \log\tau + d\log\tau$. The significance of panels and line types is the same as in Fig. 10.

models — also appears in the HI spectra, but it is less dramatic, and the downturn occurs at such low optical depth that it might be masked by errors in continuum fitting. The line models also have smaller fractions of the spectrum with transmission in the middle range $0.05 < F < 0.9$. The $P(\log\tau)$ distributions of the line models are much broader than those of the CDM models, reflecting the same trends seen in $P(F)$. Unfortunately, the strong differences in the HeII spectra are mostly lost when the spectra are smoothed over $3\mathring{A}$. The higher resolution spectra obtainable with HST may be better suited to detecting or ruling out the gaps in HeII absorption predicted by the line models, even though HST can only probe redshifts $z > 3$. Our simulations tend to underestimate the widths of $P(F)$ and $P(\log\tau)$ for the smoothed spectra because the 890 km s^{-1} filter width is a substantial fraction of our box size (2028 km s^{-1} at $z = 2.33$), and because we do not include spatial fluctuations in the intensity of the ionizing background (Zuo 1992; Fardal & Shull 1993), which could be a significant source of additional fluctuations in the HeII opacity. A comparison of CDM simulations to ground-based, HI data using the cumulative form of $P(F)$ is presented in Rauch et al. (1997) and Croft et al. (1997). For further discussion of this statistic, see Miralda-Escudé et al. (1996).

Figure 12 shows the distribution function of the log of the optical depth ratio, $\log(\tau_{\rm HeII}/\tau_{\rm HI})$. As in Figure 9, the top panels show results for unsmoothed spectra, the middle panels show results with both spectra smoothed over 890 km s^{-1}, and the bottom panels show results using smoothed spectra for $\tau_{\rm HeII}$ but unsmoothed spectra for $\tau_{\rm HI}$. Starting with the top left panel, we see that the three CDM models predict similar distributions of $\log(\tau_{\rm HeII}/\tau_{\rm HI})$, all peaked around $\tau_{\rm HeII}/\tau_{\rm HI} \approx 8$. The extended tails towards low $\tau_{\rm HeII}/\tau_{\rm HI}$ are caused by thermal broadening, and the shorter tails towards high $\tau_{\rm HeII}/\tau_{\rm HI}$ are caused by collisional ionization, as discussed in §3.3. In the smoothed spectra (middle left panel), the CCDM and OCDM models have broader distributions than the SCDM model, though the regime where this difference is strong is well below the peak of the distribution, and it may therefore be difficult to probe observationally. For smoothed HeII but unsmoothed HI (bottom left panel), the distributions become extremely broad and virtually identical. In particular, there are strong tails towards low $\tau_{\rm HeII}/\tau_{\rm HI}$ caused by strong HI features whose HeII counterparts have been reduced by smoothing. The distributions also extend to high $\tau_{\rm HeII}/\tau_{\rm HI}$ because the smoothed HeII optical depth is rarely less than 0.2, while the optical depth in the unsmoothed HI spectra can be 0.01 or smaller (see Figure 11).

Right hand panels of Figure 12 compare the SCDM model to the line models. Without smoothing, the turbulent and thermal broadening models define two extremes, both very different from the CDM results. By construction, the turbulent broadening model has a constant ratio of $\tau_{\rm HeII}$ to $\tau_{\rm HI}$, so its distribution is a δ-function at $\tau_{\rm HeII}/\tau_{\rm HI} = 17$. In the thermal broadening model, however, the HI and HeII b-parameters differ by a factor of two, so in every line the ratio $\tau_{\rm HeII}/\tau_{\rm HI}$ is high in the core and low in the wings. When the HeII and HI spectra are smoothed, the line model distributions are broader than the CDM distributions, especially in the direction of high $\tau_{\rm HeII}/\tau_{\rm HI}$. However, the strong differences again occur well below the peak of the distribution. Dividing smoothed HeII optical depths by unsmoothed HI optical depths again yields a broad

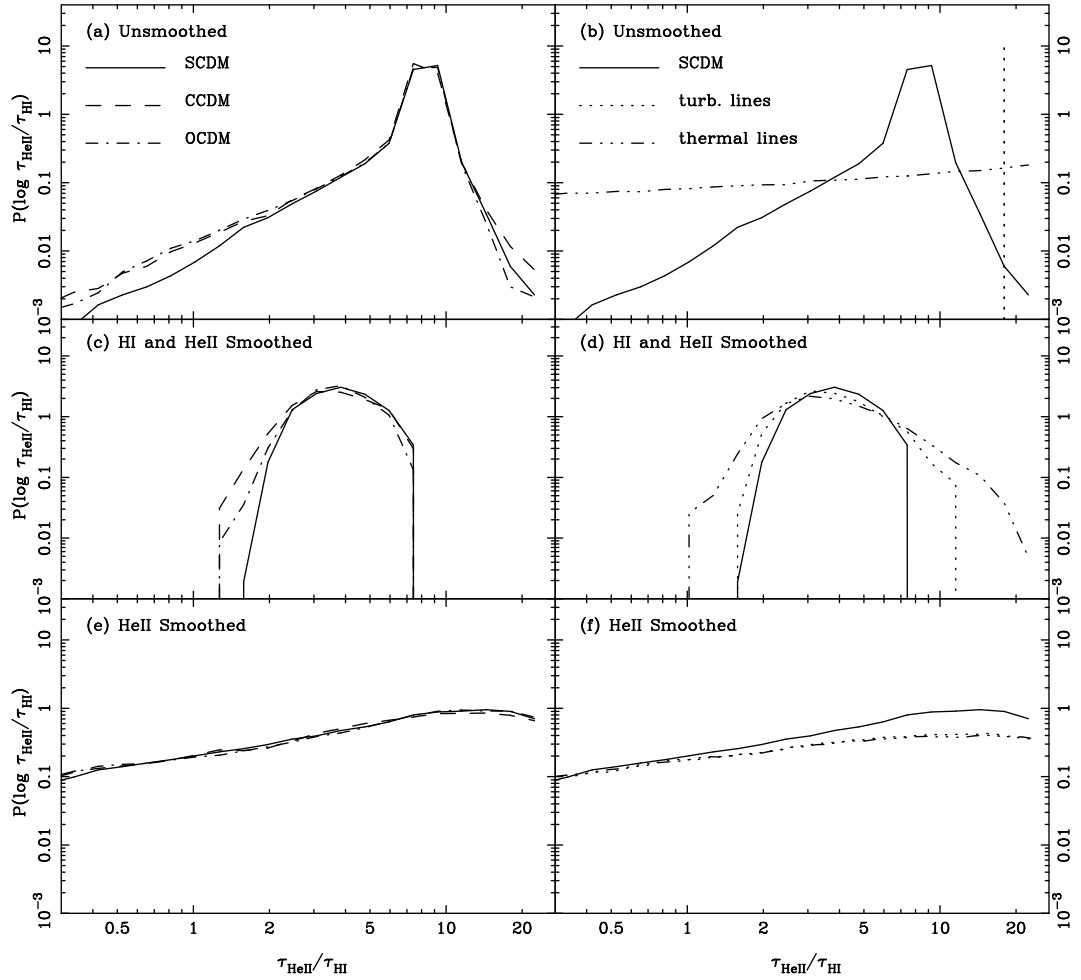

Fig. 12.— Distribution function of the log of the optical depth ratio, $\log(\tau_{\rm HeII}/\tau_{\rm HI})$, at $z = 2.33$. Layout is similar to that of Figure 9.

distribution function, but in this case the CDM results lie significantly above the line model results at the peak of the distribution, providing a clear distinction between the two sets of models. As in Figure 9, the difference reflects the presence of gaps in the line model HI spectra.

Figures 9 and 12 show two useful 1-dimensional summaries of information contained in the 2-dimensional, joint distribution of HI and HeII optical depths (Figure 5). Figure 11 shows the projections of this distribution along the HI and HeII axes. There are other potential cuts through this joint distribution, or one could use the full 2-dimensional distribution itself to distinguish between models.

Our cosmological simulations have finite resolution, as discussed in §2. The gravitational softening length, 10 kpc comoving, is much smaller than the typical scale of Lyα absorbers, but we do not adequately resolve baryonic structures less massive than ~ 32 SPH particles ($4.65 \times 10^9 M_\odot$ for SCDM and CCDM, $2.11 \times 10^9 M_\odot$ for OCDM), and we cannot represent the initial fluctuation spectrum for wavelengths smaller than twice the initial particle grid spacing, $\lambda = 350\ h^{-1}$ kpc comoving. If we simulated the same volumes with much larger particle numbers, we would therefore expect some differences of detail for the statistical results illustrated in this section. However, the regions of the IGM that dominate HeII and HI absorption are low density and fairly smooth, and they lie outside the density/temperature regime in which cooling instabilities play an important role, so we do not expect major changes in our results to appear at higher resolution. We cannot firmly estimate the quantitative impact of resolution effects until we are able to perform simulations with more particles, which will be possible with a parallel TreeSPH code now under development (Davé, Dubinski & Hernquist 1997). We expect that the main qualitative effect of increased resolution on the simulated IGM will be a larger amount of low-amplitude substructure in underdense regions. Simulations with a factor of eight *fewer* particles than the ones used here yield similar physical properties for the IGM and a similar column density distribution for HI Lyα lines with $N_{\rm HI} \lesssim 10^{15}{\rm cm}^{-2}$, but many fewer systems at higher column densities, where radiative cooling becomes important (Miralda-Escudé et al., in preparation).

The principal physical uncertainty in our simulations is the impact of reionization on gas temperatures. As pointed out by Miralda-Escudé & Rees (1994), the energy injection of one photoelectron per proton during reionization can heat the IGM to several $\times\ 10^4$K, *if* reionization occurs rapidly enough that this energy is not dissipated by collisional line cooling. Our equilibrium treatment of photoionization suppresses this heating because we set neutral fractions to low values as soon as the ionizing background switches on, without altering gas temperatures. This treatment is equivalent to assuming that reionization occurred slowly (with consequent radiative cooling) or at high redshift (with consequent heat losses to Compton and adiabatic cooling). If we instead assumed that the IGM at $z \sim 2 - 3.5$ retained significant heat from reionization, then the temperatures of the unshocked or weakly shocked gas would be higher and less dependent on density. Recall that for the gas that produces most of the absorption, the HI and HeII optical depths are proportional to $\rho_b T^{-0.7} \Gamma^{-1}$. With hotter gas, the required values of $C_{\rm HI}$ and $C_{\rm HeII}$ would therefore be higher, i.e., our models would require a less intense UV background or a

higher baryon density in order to match the observed $\overline{\tau}_{\rm HI}$ and $\overline{\tau}_{\rm HeII}$. For a fixed reionization history, the $(\Omega_b h^2)^{1.7}$ dependence in equation (8) would be closer to $(\Omega_b h^2)^2$, since the effect of reionization heating on gas temperatures does not depend on Ω_b (though the subsequent photoionization heating does). The magnitude of these effects depends on the reionization model; plausible models could increase $C_{\rm HI}$ and $C_{\rm HeII}$ by $25-50\%$ (see the discussion by Hui & Gnedin 1997). However, once the simulations were normalized to the observed $\overline{\tau}_{\rm HI}$ and $\overline{\tau}_{\rm HeII}$, we would expect the statistical properties of the absorption to be very similar to those computed here, with small changes reflecting the weaker dependence of optical depth on density and the larger degree of thermal broadening. Plausible changes in the reionization history all go in the direction of increasing rather than decreasing IGM temperatures, so they only tend to raise the lower bounds to Ω_b discussed in §3.2. IGM temperatures and corresponding Ω_b limits could be lower if the UV background spectrum is substantially softer than the HM spectrum, so that the mean residual photoelectron energy is lower.

4. Conclusions

Many previous discussions of HeII absorption have focused on distinguishing "line blanketing" in the Lyα forest from "Gunn-Peterson" absorption by the IGM. Our cosmological simulations undermine the premise of this effort, for they suggest that HeII absorption and the low column density Lyα forest *both* arise in diffuse, smoothly fluctuating, intergalactic gas. Local maxima in the optical depth can be identified as lines, but individual features do not, as a rule, correspond to compact structures that are sharply separated from their environment. While the Lyα forest and the HeII flux decrement are both manifestations of the IGM, the high ratio of HeII ions to HI atoms does lead to an important systematic difference between helium and hydrogen absorption: HeII absorption is stronger in the mean, and much of it arises in underdense regions that have low HI optical depth. The general picture of the IGM presented here is similar to that in the other numerical simulation papers cited in the introduction, and it has much in common with the semi-analytic models developed by Bi (1993), Bi, Ge, & Fang (1995), Bi & Davidsen (1997), and Hui, Gnedin, & Zhang (1997). These semi-analytic models lead to similar qualitative conclusions about the properties of the gas producing HeII absorption (Davidsen, private communication; Davidsen et al., in preparation).

Some of the more specific conclusions from our analysis are as follows:
(1) The CDM models account for the observed relative values of $\overline{\tau}_{\rm HI}$ (from PRS) and $\overline{\tau}_{\rm HeII}$ (from DKZ and HAR) if the UV background has the spectral shape predicted by HM. Large changes in the spectral shape (or in the observational estimates) would spoil this agreement.
(2) These models account for the observed absolute values of $\overline{\tau}_{\rm HI}$ and $\overline{\tau}_{\rm HeII}$ only if (a) the overall intensity of the background is lower than predicted by HM, or (b) the baryon density is higher than our assumed value of $\Omega_b h^2 = 0.0125$. If we set the background intensity equal to the HM value, then the SCDM and OCDM models require $\Omega_b h^2 \approx 0.023$, and the CCDM model

requires $\Omega_b h^2 \approx 0.038$. We have analyzed one SCDM simulation with a higher baryon density, $\Omega_b h^2 = 0.03125$. If $\Gamma_{\rm HeII}$ is held fixed, then this model produces stronger HeII absorption than the original SCDM model, as expected. Once both models are normalized to produce the same $\overline{\tau}_{\rm HeII}$, the statistical properties of their HeII absorption (e.g., the measures considered in §3.4) are virtually identical.

(3) The CDM models naturally explain the observed evolution of $\overline{\tau}_{\rm HeII}$, in particular the factor of two drop in $\overline{\tau}_{\rm HeII}$ between $z \approx 3.3$ (HAR) and $z \approx 2.4$ (DKZ), provided $\Gamma_{\rm HeII}$ evolves at the rate calculated by HM. Change in the UV background does not play a major role in this evolution — $\Gamma_{\rm HeII}$ grows by only 20% between $z = 3.3$ and $z = 2.4$. The strong evolution of $\overline{\tau}_{\rm HeII}$ is instead driven by the expansion of the universe, which lowers gas densities and spreads absorbing material over larger frequency ranges. The high HeII optical depth measured by HAR does not imply that HeII reionization occurred at $z < 3.3$. If the HAR upper limit of $\overline{\tau}_{\rm HeII} < 3.0$ outside the Q0302-003 ionization zone is correct, then the photoionizing background along this line of sight cannot be much softer than HM predict.

(4) Most of the HeII opacity is produced by diffuse gas that follows a well defined relation between temperature and density. This relation has its origin in the competition between photoionization heating and adiabatic cooling. For gas that lies on this temperature-density relation, the HeII optical depth is a simple function of density, $\tau_{\rm HeII} \propto \rho_b^{1.6}$. To a first approximation, one can regard a HeII (or HI) absorption spectrum as a non-linear map of the gas density along the line of sight.

(5) A significant fraction of the HeII absorption arises in regions with density contrast $\delta \leq -0.5$, for which linear perturbation theory will give inaccurate results. Analytic methods that treat this density regime more accurately, such as the Modified Zeldovich Approximation of Reisenegger & Miralda-Escudé (1995), may provide useful guides to the behavior of HeII absorption in cosmological models, especially in light of point (4) above.

(6) The three CDM models that we have investigated predict similar statistical properties of the HeII absorption (e.g., distribution functions of $\tau_{\rm HeII}$ and $\tau_{\rm HeII}/\tau_{\rm HI}$), once they are normalized to produce the same mean absorption. The CCDM model predicts somewhat broader distribution functions than the SCDM or OCDM models because of its higher mass fluctuation amplitude. Because this model has emptier voids, it also requires a lower UV background intensity and/or higher $\Omega_b h^2$ to reproduce the observed $\overline{\tau}_{\rm HeII}$, and it requires a slightly softer background spectrum to account simultaneously for $\overline{\tau}_{\rm HI}$ and $\overline{\tau}_{\rm HeII}$. On the scales of our simulation, the three CDM models have power spectra of similar shapes, and their rms fluctuation amplitudes differ by less than a factor of two, so we do not yet know how the absorption results might change for much steeper or shallower power spectra or for models that have very different fluctuation amplitudes on these scales.

(7) The CDM models have very different HeII absorption properties from our "line models," which assume that the HeII absorption is produced by randomly distributed, Voigt-profile lines with $dN/dN_{\rm HI} \propto N_{\rm HI}^{-1.5}$ and a lower cutoff at $N_{\rm HI} = 10^{12}$ cm^{-2}. In particular, the line models have gaps in which the HeII absorption is very low, and a larger fraction of their HeII absorption arises in regions of high HI optical depth. The fluctuating IGM of the CDM models produces fluctuating

HeII absorption, but absorption-free regions ($\tau_{\rm HeII} \lesssim 0.05$) are very rare. The line models require a softer UV background spectrum in order to produce the observed $\overline{\tau}_{\rm HeII}$, especially if the lines are thermally broadened. The statistical differences between the line models and the CDM models are greatly reduced when the spectra are smoothed, so for distinguishing these scenarios it is desirable to use HeII spectra with the highest resolution practical. If the minimum column density in the line models is pushed well below 10^{12} cm^{-2}, the differences from the CDM models are less striking, as weak lines overlap to produce a continuous, fluctuating background.
(8) About half of the contribution to $\overline{\tau}_{\rm HeII}$ comes from regions that have $\tau_{\rm HI} < 0.15$. In the CDM models, most of the absorption in this regime is produced by a smoothly fluctuating IGM rather than the wings of strong absorption lines. The absorption is not uniform, but because the HI optical depth is low and the variations are gentle, much of the corresponding HI absorption could be inadvertently removed from optical quasar spectra in the process of continuum fitting.

The CDM simulations provide a model of the high redshift IGM. Once it is normalized to the observed values of $\overline{\tau}_{\rm HeII}$ and $\overline{\tau}_{\rm HI}$, this model yields a number of testable predictions. First, the shape of the UV background spectrum should be close to that predicted by HM, with $\Gamma_{\rm HI}/\Gamma_{\rm HeII} \approx 100$, for $2 \lesssim z \lesssim 3.3$. It is difficult to measure the background shape precisely independent of an IGM model, but tests using metal line ratios (Songaila & Cowie 1995) or comparisons of the HI and HeII proximity effects (see Zheng & Davidsen 1995) might be able to identify strong departures from the HM spectral shape. If one adopts the intensity of the HM background as a lower limit, then our models also predict that the baryon density exceeds the "conventional" big bang nucleosynthesis estimate of $\Omega_b h^2 = 0.0125$ by a factor $\sim 1.5-3$ (see Rauch et al. 1997 and Weinberg et al. 1997 for further discussion). The most direct and quantitative predictions of this IGM scenario are statistical properties of the absorption such as those shown in §3.4. In particular, observational analyses can test the predictions that a large fraction of the HeII opacity arises in regions of low HI optical depth and that there are few regions where $\tau_{\rm HeII}$ itself is very low. The DKZ spectrum offers the largest redshift range for statistical analyses of HeII absorption. However, the distinctive features of this IGM model are most stringently tested at high spectral resolution, so HST observations at $z > 3$ can also play an important role. An anecdotal but significant argument in favor of this IGM model is provided by HAR, who show that strong HeII absorption ($\tau_{\rm HeII} > 1.3$) persists in a region where a Keck HIRES spectrum reveals no HI Lyα lines down to a detection threshold $\tau_{\rm HI} = 0.05$.

Careful comparison between the simulations and HeII observations should include realistic treatments of noise, instrumental resolution, the redshift range of the observations, and so forth. The three variants of the CDM model considered in this paper yield fairly similar predictions, and given the inevitable limitations of HeII measurements with existing instruments, we anticipate that HI observations will be a more powerful tool for distinguishing among them. However, HeII absorption provides a vital test of this general scenario for high redshift structure, checking one of its basic predictions in a regime that is almost inaccessible to other methods. In theories of structure formation like those studied here, underdense regions of the universe harbor a substantial

amount of diffuse baryonic material. If these theories are even roughly correct, then the recent studies of HeII absorption in quasar spectra have detected this material at high significance. More detailed analyses of existing absorption data can test this claim. Future instruments that can observe HeII absorption at high spectral resolution could yield a precise view of structure in the sparsest regions of the high-redshift universe.

Acknowledgements

We acknowledge inspiring talks by Peter Jakobsen and Arthur Davidsen on HeII absorption observations at an STSci workshop on QSO absorption lines in June, 1995. We thank Arthur Davidsen, Craig Hogan, Jordi Miralda-Escudé, and Andreas Reisenegger for stimulating and informative discussions about HeII absorption. We thank Piero Madau for helpful discussions on the UV background and for providing the HM background spectrum in convenient numerical form. We also thank Jordi Miralda-Escudé for providing us with the computer program used to generate the line model spectra. The simulations were performed at the San Diego Supercomputer Center. This work was supported by NASA Astrophysical Theory Grants NAG5-2864, NAG5-3111, NAGW-2422, NAG5-2793, by NASA Long-Term Space Astrophysics Grant NAG5-3525, by NASA HPCC/ESS grant NAG5-2213, and by the NSF under grants ASC93-18185 and the Presidential Faculty Fellows Program.

REFERENCES

Bajtlik, S., Duncan, R.C., Ostriker, J. P. 1988, ApJ , 327, 570

Bennett, C., L., Banday, A. J., Gorskí, K. M., Hinshaw, G., Jackson, P., Keegstra, P., Kogut, A., Smoot, G. F., Wilkinson, D. T., Wright, E. L. 1996, ApJ, 646, L1

Bi, H. 1993, ApJ , 405, 479

Bi, H., & Davidsen, A. F. 1997, ApJ , 479, 523

Bi, H., Ge, J., & Fang, L.-Z. 1995, ApJ , 452, 90

Carswell, R. F., Rauch, M., Weymann, R. J., Cooke, A.J., Webb, J.K., 1994, MNRAS , 268, L1

Cen, R., Miralda-Escudé, J., Ostriker, J.P., Rauch, M., 1994, ApJ, 437, L9

Croft, R. A. C., Weinberg, D. H., Hernquist, L. & Katz, N., 1997, in Proceedings of the 18th Texas Symposium on Relativistic Astrophysics, eds. Olinto, A., Frieman, J. & Schramm, D., World Scientific), astro-ph 9701166

Davé, R., Dubinski, J., Hernquist, L., 1997, New Astronomy, submitted, astro-ph 9701113

Davé, R., Hernquist, L., Weinberg, D. H., Katz, N. 1997, ApJ , 477, 21

Davidsen, A.F., Kriss, G. A. & Zheng, W., Nature, 380, 47 (DKZ)

Efstathiou, G., Bond, J. R., & White, S. D. M., 1992, MNRAS , 258, 1p

Fardal, M. A., & Shull, M. J. 1993, ApJ , 415, 524

Giallongo, E., Cristiani, S., Dodorico, S., Fontana, A., Savaglio, S., 1996, ApJ , 466, 46

Giroux, M.L., Fardal, M.A., & Shull, J.M. 1995, ApJ , 451, 477

Gorski, K. M., Ratra, B., Sugiyama, N., & Banday, A. J. 1995, ApJ , 444, L65

Gunn, J. E. & Peterson, B. A. 1965, ApJ , 142, 1633

Haardt, F. & Madau, P. 1996, ApJ , 461, 20 (HM)

Hellsten, U., Davé, R., Hernquist, L., & Katz, N., 1997, ApJ , in press, astro-ph 9701043

Hernquist, L. & Katz, N. 1989, ApJS, 70, 419

Hernquist, L., Katz, N., Weinberg, D.H., Miralda-Escudé, J., 1996, ApJ , 457, L51 (HKWM)

Hogan, C.J., 1997, in Proceedings of the 18th Texas Symposium on Relativistic Astrophysics, eds. Olinto, A., Frieman, J. & Schramm, D., World Scientific).

Hogan, C.J., Anderson, S.F. & Rugers, M.H. 1996, AJ, in press (HAR)

Hu, E.M., Kim, T.-S., Cowie, L.L., Songaila, A. & Rauch, M. 1995, AJ, 110, 1526

Hui, L., & Gnedin, 1996, MNRAS , submitted, astro-ph/9612232

Hui, L., Gnedin, N. Y., & Zhang, Y. 1997, ApJ , in press, astro-ph/9608157

Jakobsen, P., Boksenberg, A., Deharveng, J. M., Greenfield, P., Jedrzejewski, R., Paresce, F. 1994, Nature, 370, 35 (JBDGJP)

Katz, N., Weinberg, D.H. & Hernquist, L. 1996, ApJS, 105, 19 (KWH)

Lynds, C.R. 1971, ApJ, 164, L73

Madau, P., & Meiksin, A. 1994, ApJ, 433, L53

Miralda-Escudé, J. 1993, MNRAS , 262, 273

Miralda-Escudé,J., Cen, R., Ostriker, J.P. & Rauch, M., 1996, ApJ , 471, 582

Miralda-Escudé, J., & Ostriker, J. P. 1992, ApJ , 392, 15

Miralda-Escudé, J., & Rees, M. J. 1993, MNRAS , 260, 617

Miralda-Escudé, J., & Rees, M. J. 1994, MNRAS , 266, 343

Press, W., H., Rybicki, G. B., & Schneider, D. P. 1993, ApJ , 414, 64 (PRS)

Rauch, M., Miralda-Escudé, J., Sargent, W. L. W., Barlow, T. H., Weinberg, D. H., Hernquist, L., Katz, N., Cen, R., Ostriker, J. P. 1997, ApJ , submitted, astro-ph 9612245

Reisenegger, A. & Miralda-Escudé, J. 1995, ApJ , 449, 476

Rugers, M., & Hogan, C.J. 1996, ApJ, 459, L1

Rugers, M., & Hogan, C.J. 1996b, AJ, 111, 2135

Sargent, W.L.W., Young, P.J., Boksenberg, A., Tytler, D. 1980, ApJS, 42, 41

Songaila, A. & Cowie, L.L. 1996, AJ, 112, 335

Songaila, A. & Cowie, L.L., Hogan, C.J., Rugers, M. 1994, Nature, 368, 599

Songaila, A., Hu, E. M., & Cowie, L.L. 1995, Nature, 375, 124

Songaila, A., Wampler, E. J., & Cowie, L.L. 1997, Nature, 385, 137

Tytler, D., Fan, X. & Burles, S. 1996, Nature, 281, 207

Tytler, D., Burles, S., & Kirkman, D., 1996, ApJ , submitted, astro-ph 9612121

Walker T. P., Steigman, G., Schramm, D. N., Olive, K. A., Kang, H. S., 1991, ApJ , 376, 51

White, S. D. M., Efstathiou, G. P. & Frenk, C. S. 1993, MNRAS , 262, 1023

Weinberg, D.H., Hernquist, L., & Katz, N. 1997, ApJ , 477, 8

Weinberg, D.H., Miralda-Escudé, J., Hernquist, L., & Katz, N., 1997, ApJ , submitted, astro-ph 9701012

Zhang, Y., Anninos, P., Norman, M.L. 1995, ApJ, 453, L57

Zhang, Y., Anninos, P., Norman, M.L., Meiksin, A. 1996, ApJ , submitted, astro-ph 9609194

Zheng, W., & Davidsen, A. 1995, ApJ, 440, L53

Zuo, L. 1992, MNRAS, 258, 36

Zuo, L. & Lu, L. 1993, ApJ , 418, 601